## Title

Experimental investigation into coal wettability changes caused by reactions with scCO2-H2O



## Authors

Li, Ke
Zhu, Chuanjie
Wan, Jiamin
et al.

## Publication Date

2024-08-01

## DOI

10.1016/j.jgsce.2024.205366

Peer reviewed

# Experimental investigation into causes of coal surface wettability variation resulting from reaction with $scCO_2$-$H_2O$

Ke Li [a], Chuanjie Zhu [a*], Jiamin Wan [b], Tetsu K. Tokunaga [b], Na Liu [a], Cong Ma [a], Baiquan Lin [a]

[a] Faculty of Safety Engineering, China University of Mining and Technology, Xuzhou, Jiangsu, 221116, China; [b] Earth and Environmental Sciences Area, Lawrence Berkeley National Laboratory, Berkeley, CA, 94720, USA.

[*]Corresponding author: Chuanjie Zhu, E-mail: anq021@126.com

**Abstract:** Geological $CO_2$ sequestration (GCS) can help mitigate global warming and enhance methane recovery from coal beds. However, few studies have linked the effects of $CO_2$ to surface chemistry changes controlling wetting behavior in deep coal beds. Contact angles (CAs) of $CO_2$/$N_2$-high volatile bituminous coal-$H_2O$ systems were measured under different temperatures and pressures. The surface chemistry and physical structure of coals were characterized to investigate changes in physicochemical properties and their relations with wettability after reactions. For $N_2$ treatment, changes in CAs were insignificant. For gaseous $CO_2$ treatment, the static CA and the average advancing angle increased slightly. With supercritical (sc) $CO_2$, both the static and dynamic CAs increased significantly, and $\theta_{adv}$ changed to intermediate-wet (92°). Reactions with minerals exposed to $scCO_2$ resulted in greater surface roughness and inhomogeneity, greater contact angle hysteresis and more surface sites occupied by $scCO_2$ rather than $H_2O$. Increases in hydrophobic functional groups and decreases in hydrophilicity were shown by FTIR spectra, reflecting the shedding of polar oxygen-containing functional groups, reduction of hydrogen bonds, and increasing percentage of hydrocarbons. XRD patterns obtained following $scCO_2$-treatment showed that crystallite growth and molecular polymerization were higher toward graphite-like. The calculated structural parameters of functional groups and crystallites both showed elevated coal rank. ~~The changes~~ Changes ~~of~~ in crystallite structure~~,~~ ~~represent~~ notably higher carbon content and decreased negative surface charge, ~~which~~ are unfavorable for water-wetting. This study contributes to understanding surface chemistry changes responsible for decreased wettability during $CO_2$-enhanced coal bed methane recovery and GCS in coal reservoirs.

## Highlights

(1) Wettability of coal treated by $scCO_2$ changed significantly but not by gas-$N_2$/$CO_2$ and $scN_2$.

(2) Under $scCO_2$ treatment, static contact angle changes stabilized at after 48 hours.

(3) $ScCO_2$ treatment decreased abundance of hydrophilic functional groups.

(4) Rougher surface caused by $scCO_2$ treatment generated greater contact angle

hysteresis.
(5) $ScCO_2$ treatment depleted the inorganic minerals in coal (most notably calcite).

**Keywords:** High volatile bituminous coal; Wetting; Contact angle; Supercritical $CO_2$; Functional groups; Minerals; Crystallite structure

## Graphical abstract

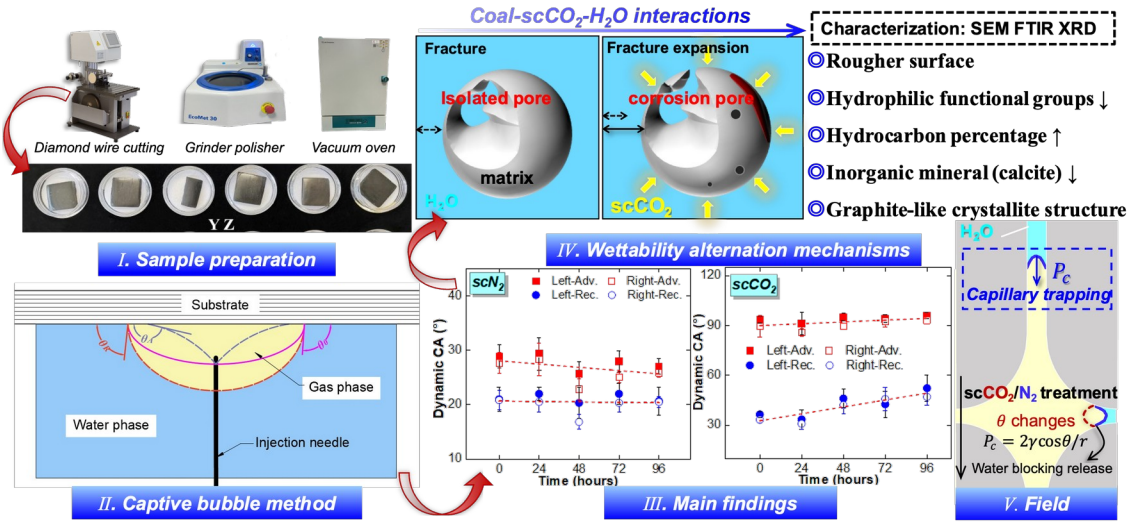


# 1 Introduction

Geological $CO_2$ sequestration (GCS) in coal beds ~~has~~ provides advantages of $CO_2$ storage and enhanced coal bed methane recovery ($CO_2$-ECBM) (Hadi Mosleh et al., 2017). Thus $CO_2$ enhanced oil recovery ($CO_2$-EOR) and $CO_2$-ECBM are widely studied and commercially applied (Godoi and Matai, 2021). $CO_2$-ECBM has unique advantages resulting from coal matrix micropore development that favors adsorption of $CO_2$ relative to $CH_4$ (X. Liu et al., 2023). Thus, adsorption trapping is the most prominent trapping mechanism in coal reservoirs (Iglauer, 2011). Wettability is an important factor which affects the potential and efficiency of $CO_2$ trapping and methane recovery as shown in **Figure 1** (**Tokunaga et al., 2013**).

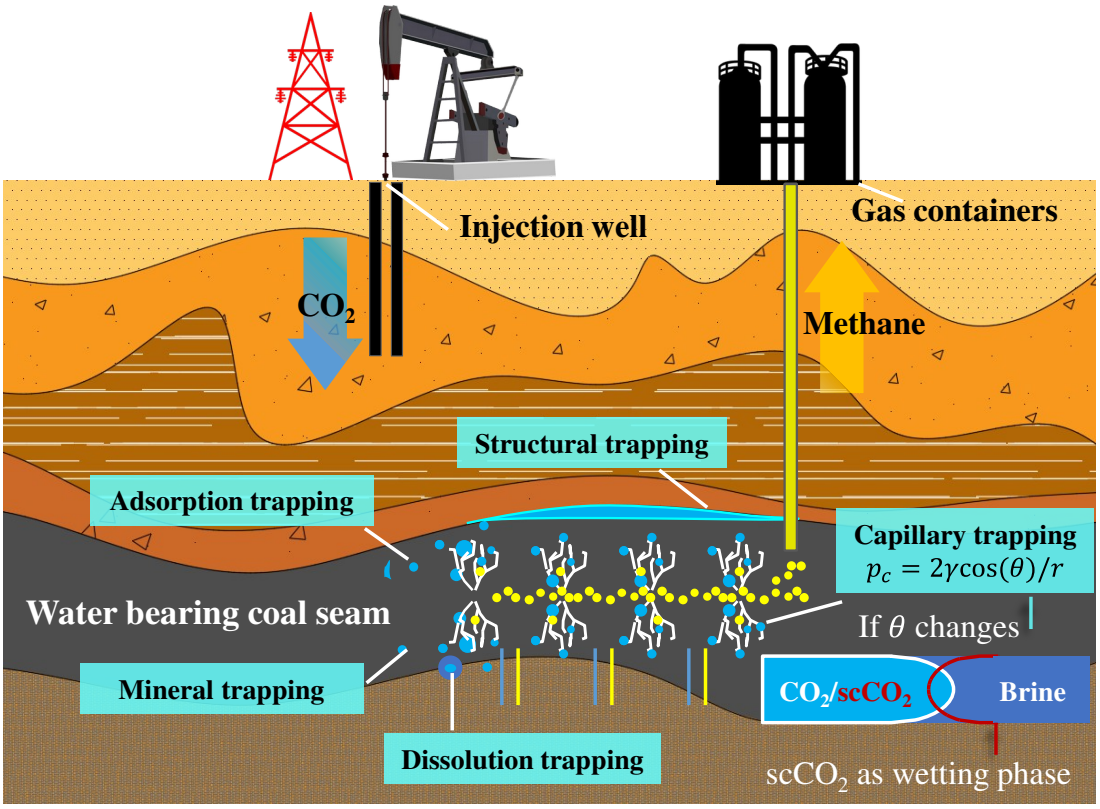


**Figure 1** GCS with five main trapping mechanisms and $CO_2$-ECBM in deep coal reservoirs, where the efficiency of geological storage (especially capillary and structure trapping) and methane recovery displacement depend on wettability.

Minerals show different affinities for $H_2O$ and wettability becomes complicated after $CO_2$ injection into water-bearing reservoirs (Fatah et al., 2021a). Previous studies reported on the wettability of $CO_2$-treated minerals (Jung and Wan, 2012; Sun and Bourg, 2023; Tenney and Cygan, 2014), ~~i.e.,~~in particular mica (muscovite), quartz or silica, feldspar, calcite, kaolinite, smectite. For coal which ~~consists~~ is composed of multiple mineral~~s composition~~ as shown in Table A. 1, wettability is also affected by coal rank and mineral component content (Arif et al., 2016b; Shojai Kaveh et al., 2012), which reflect differences in physicochemical properties of surfaces.

Wettability has been widely investigated as a function of reservoir conditions (temperature, pressure, salinity, ion type/strength, and fluid composition) (Shojai Kaveh et al., 2016, 2011). Arif et al. (2016a) reported that the advancing and receding angles of mica (surface roughness ~12 nm) exposed to $CO_2$ were positively correlated with pressure and salinity, and negatively correlated with temperature. The advancing contact angle (CA) at 20 MPa and 308 K was ~110°, and water-wet surfaces became $CO_2$-wet. Iglauer et al. (2012) used molecular dynamics to simulate contact angles in $CO_2$-$H_2O$/NaCl-quartz systems as a function of pressure at 300 K and 350 K, and reported that contact angles increased significantly with pressure and weakly with salinity at subcritical ~~or~~ and supercritical states. Chen et al. (2015) investigated contact

angles of quartz under different ionic strengths (divalent ion $Ca^{2+}$ and monovalent ion $Na^{+}$). Ibrahim and Nasr-El-Din (2016) measured the zeta potential of high volatile bitumen coal (hvBb) under different NaCl concentrations by a phase-analysis light-scattering technique. Roshan et al. (2016) conducted experiments under various ion types (NaCl, KCl, $MgCl_2$, $CaCl_2$) and concentrations (0.1, 0.5, and 1 M). Zheng et al. (2020) used nuclear magnetic resonance (NMR) as a non-invasive method to study effects of water status (adsorbed-water, free-water) on wettability, and found that free-water decreased $CO_2$ wetting and the sensitivity of wettability to pressure.

Previous work explained wettability mainly through influences of molecular density (Arif et al., 2016a), pore adsorption (Sun et al., 2022), interfacial tension, surface charge, and organic matter (Shojai Kaveh et al., 2012). The increase of molecular density implied that the probability of collision increases between $H_2O$ molecules and C molecules (Liu et al., 2010), and $H_2O$ molecules are more likely to be trapped on the surface. Zhu et al. (2019) reported that the dependence of adsorption isotherms on temperature and pressure is consistent with changes in the contact angle. Equilibrium contact angle can be calculated by combining the interfacial tension (IFT) values between different phases with the modified equation of state (EOS) and Young-Laplace equation (Shojai Kaveh et al., 2016). However, while adsorption and interfacial tension are parameters correlated with wettability, it is desirable to identify underlying mechanisms. The reduction of negative surface charge decreases electrostatic repulsions (electric double layer theory (Tokunaga, 2012)), which consequently affects water film stability and wettability. Fatah et al.(Fatah et al., 2021a) reported that $scCO_2$ may dissolve clay and carbonate minerals and transform the clay-rich shale to become $CO_2$-wet. Arain et al. (2023) reported that trace amounts of hydrocarbons on coal surfaces like dissolved organic matter (Ali et al., 2022) altered wettability of rocks. Crawford et al. (1994) concluded that the effect of oxygen-containing functional groups on wettability cannot be ignored. Gathitu et al. (2009) found that coal exposed to $CO_2$ may lead to new carbon structure and rearrange macromolecules.

Previous work evaluated wettability of various minerals as a function of reservoir conditions. However, studies on the mechanisms of wettability alteration of coal exposed to $scCO_2$-$H_2O$ are limited, and few have ~~currently~~ linked wetting behavior with surface chemistry. The surface wettability is complex due to the differences in structure and components between coal and pure, natural minerals. Furthermore, the interactions between coal and $CO_2$-$H_2O$ also affect the wettability. Wettability variations introduce a large uncertainty into the prediction of trapping $CO_2$, methane displacement capacity, $CO_2$ storage height, and $CO_2$ containment security. Therefore, it is crucial to ~~comprehend~~ determine the potential effects of chemical reactions on wettability and the changes in physical structure (porosity, roughness) and surface chemistry (functional groups, crystal structure) of coal surface. ~~This possible wettability variations introduce a large uncertainty into the prediction of trapping $CO_2$ or displacement methane capacity and containment security.~~

In this work, we measured in-situ static/dynamic contact angles of high volatile B bituminous (hvBb) medium rank coal ~~for~~ under $N_2/CO_2$ treatment ~~under~~ at different temperatures, pressures, and exposure times to determine ~~whether~~ the extent to which changing ~~chemical reaction~~these conditions alter ~~affects~~ wettability. We then analyzed ~~the effect of chemical reaction on wettability from~~ physicochemical properties via characterization methods (FTIR, XRD, SEM) in order to identify underlying surface processes responsible for wettability alteration. This study provides measurements-based theoretical guidance for field practices, including the choice of solvents or nanofluids injected to improve $CO_2$ trapping, and further deepens the understanding of wetting behavior to enhance $CO_2$-ECBM and GCS.

## 2 Experiments

### 2.1 Experimental method and materials

#### 2.1.1 Coal sample and preparation

A high volatile B bituminous (hvBb) medium rank coal was collected from Yuanzhuang (YZ) coal mine in Huaibei, China. The proximate analysis of coal samples is shown in **Table 1**. The coal samples were prepared by block-cutting method, i.e., large coal blocks were cut into smaller square slices with dimensions of ~21mm×21mm×3-4mm (thickness), and then coal surfaces were ground and polished. Some prepared coal samples are shown in **Figure 2a**.

Coal surfaces ~~was~~ were polished with a series of silicon carbide sandpapers (220-3000 grit). Small scratches were first removed with 220-320 grit sandpapers, followed by careful water polishing with 400-3000 grit sandpapers to complete the sample surface preparation. We used deionized water to reduce surface charge interference. Sample surfaces were finally cleaned with AccuDuster III 2510 before experiments. ~~We used deionized water to reduce interference from surface charges.~~

**Table 1** Proximate analysis results of coal sample.

| Coal sample | $M_{ad}$ (%) | $A_{ad}$ (%) | $V_{daf}$ (%) | $FC_{ad}$ (%) | Coal type |
|---|---|---|---|---|---|
| **YZ** | 2.58 | 9.16 | 36.75 | 57.46 | hvBb coal |

Note: $M_{ad}$—the moisture content on air-dried basis, $A_{ad}$—the ash content on air-dried basis, $V_{daf}$—the volatile matter content on dry-ash-free basis, $FC_{ad}$—the fixed carbon content on air-dried basis.

#### 2.1.2 Contact angle measurement

Dynamic and static contact angle (CA) measurements are commonly measured by three main methods: sessile drop (Drelich, 2013), pendant drop (Bhutani et al., 2012), and captive bubble (Chau, 2009). We used the captive bubble method to measure CAs (**Figure 2b**), where bubbles were captured beneath a solid substrate submersed in the aqueous phase under precise control of $P/T$ (Wan et al., 2014). Due to ~~the~~ surface ~~inhomogeneity~~ heterogeneity of substrates, we measured advancing/receding angles (

$\theta_A$¿$\theta_R$) on both the left and right sides as shown in **Figure 2b**. The CAs reported in this study were all water contact angles, which are measured between the solid-water and nonaqueous fluid-water interfaces. After a bubble captured by the coal substrate separated from the injection needle, we began to photographically record images, which were later processed with Image J to measure static CAs.

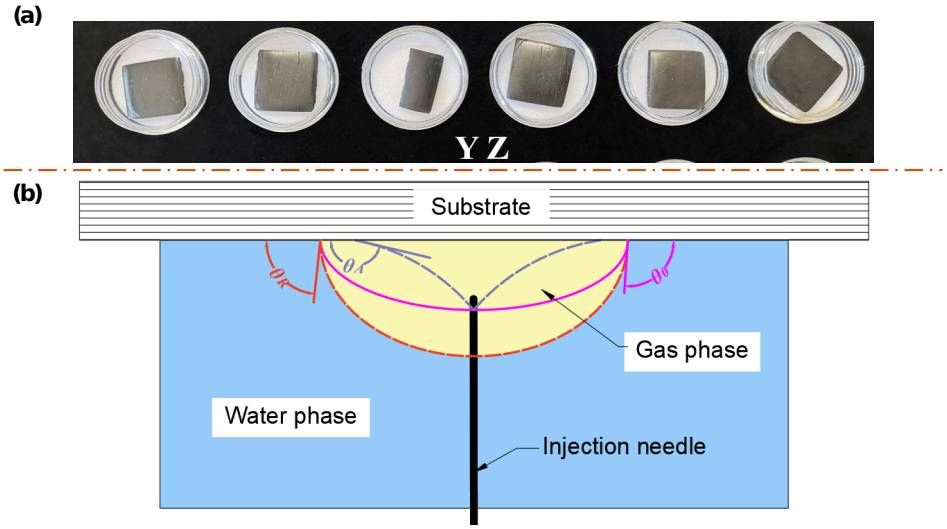


**Figure 2** Experimental samples and contact angle measurement. (a) Polished YZ coal samples ~~YZ~~, (b) Schematic of contact angle measurement by the captive bubble method. Young's equilibrium contact angle ¿$\theta_0$, advancing contact angle ¿$\theta_A$, receding contact angle ¿$\theta_R$. Usually, $\theta_A$>$\theta_0$>$\theta_R$, thus $\theta_0$ is constrained by $\theta_A$ and $\theta_R$.

## 2.2 Experiment setup and procedure

### 2.2.1 Experiment setup

The experimental system shown in **Figure 3** includes: a high pressure and temperature (P-T) chamber, stirred reactor, pressure control unit (pump, gas cylinder), temperature control unit (temperature controller, thermocouple, heat lamp, circulation fan, and thermal insulation), and experimental information acquisition unit (camera, computer, and light illuminator).

The high P-T viewing chamber (IFT-10, Core Laboratories) can support a maximum working pressure and temperature of 690 bar and 450 K, respectively. An inlet in the upper portion of the chamber is connected to a two-stem manifold (A), one of which is connected to an exhaust pipe to safely vent $CO_2$ into the ventilation ducts, and the other is connected to a pump (A) that provides back pressure. The bottom of the viewing chamber has two inlets, one of which is connected to a needle valve to generate $CO_2$ bubbles. The needle valve is connected to pump (B) via a three-way valve for controlling the flow rate of $CO_2$. The other inlet is connected to a two-stem manifold (B) which connects a stirred reactor and a water tank.

Coal samples are placed on a stainless-steel plate near the upper center of the viewing chamber. Two glass windows that are resistant to high temperature and pressure are installed on opposite sides of the chamber to enable transmission of the

illuminator's light into the chamber for recording images of the droplets. The entire experimental system is enclosed ~~by~~ in a thermally insulated ~~wall~~ box to maintain a constant temperature regulated by a temperature controller ~~regulates~~.

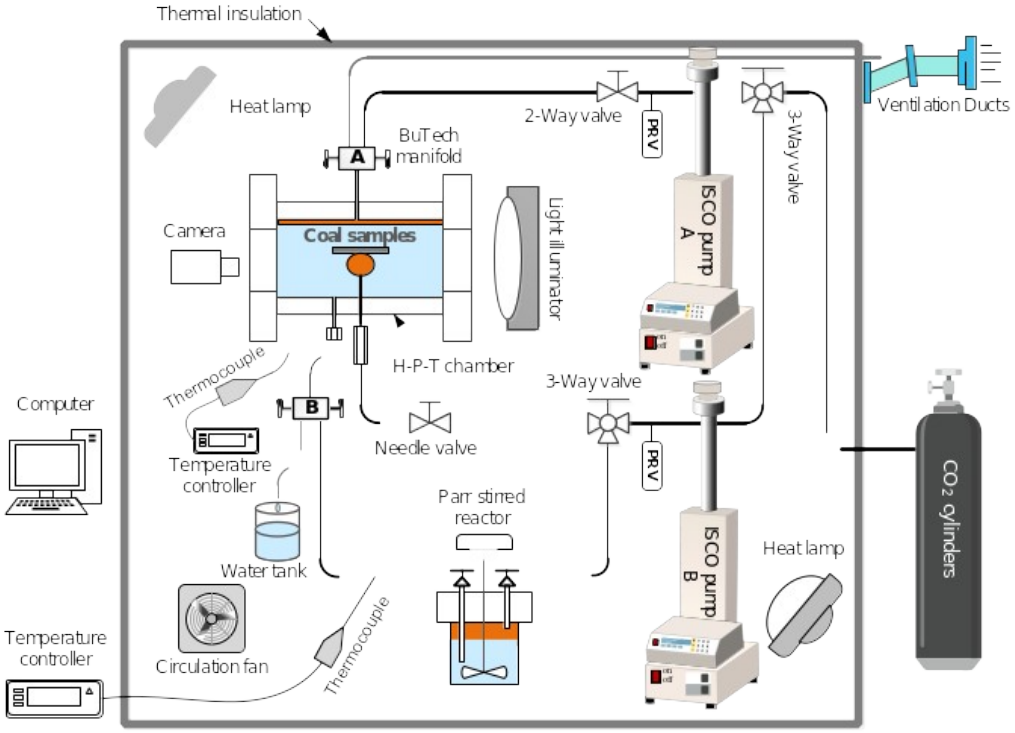


**Figure 3** Schematic diagram of the experimental systems and photographs of the experimental setup for contact angle measurements.

2.2.2 Contact angle measurement procedures

(a) Preparation before $CO_2$ releasing. We clamped a coal substrate onto the lower surface of a stainless-steel plate, and then immersed it in high pressure deionized water (20 bar) for a minimum of 48 hours to fill its pores with water. The thermally insulated box and viewing chamber were then heated to the desired temperature. The viewing chamber was pressurized to the desired pressure using pump (A) with $CO_2$.

The reactor was equilibrated to fully dissolve $CO_2$ in water, then further stirred for

30 minutes in preparation for transfer of $CO_2$-saturated water into the viewing chamber. The two pumps were set ~~in~~ to a constant pressure difference between injection pressure and back pressure. We then opened the valve between the stirred reactor and the viewing chamber to allow $CO_2$-saturated deionized water to flow into the chamber and displace the original water. Solubility equilibrium was again established for more than 1 hour.

(b) $CO_2$ captured by coal substrate. $CO_2$ bubbles were released from the stirred reactor through the needle valve and captured upon buoyant contact against the overlying coal substrate. In order to measure dynamic contact angles, the $CO_2$ bubbles advanced through the pressure difference between the reactor and the viewing chamber, and receded through lowering the pressure of the pump (B). The rate of expansion and contraction of the bubbles was controlled with the needle valve.

After each measurement, the pressure chamber was tilted to remove the captured $CO_2$ bubbles from the substrate. After a period of reaction, new $CO_2$ bubbles were then released at the same position after dissolution equilibrium. More detailed experiment procedures can be found in our previous work (Zhu et al., 2019).

**2.3 Characterization methods of physicochemical property**

(1) Surface functional group

The surface functional group chemistry of coal surfaces was measured by Fourier Transform Infrared spectroscopy (FTIR) using VERTEX 80v (Germany, Bruker) as shown in **Figure 4a**. The measurement was conducted by attenuated total reflection (ATR).

(2) Coal surface micromorphology

Surface micromorphological ~~characterization~~ of the coal samples was ~~measured~~ characterized by scanning electron microscopy (FEI Quanta TM 250, **Figure 4b** with a magnification of 6–100 million ~~times~~ and an accelerating voltage of 0.2–30 kV).

(3) Crystallite structure

Coal is a long-range disordered and short-range ordered amorphous crystal. Information on the size, shape, and structure of the ordered crystallite structure can be calculated by diffraction intensity and diffraction angle. The samples were dried to remove water in a vacuum oven before characterization~~, then~~. ~~the crystallite~~ Crystallite structures of coal were then determined by X-ray diffraction (XRD, Bruker, D8 Advance, **Figure 4c**).

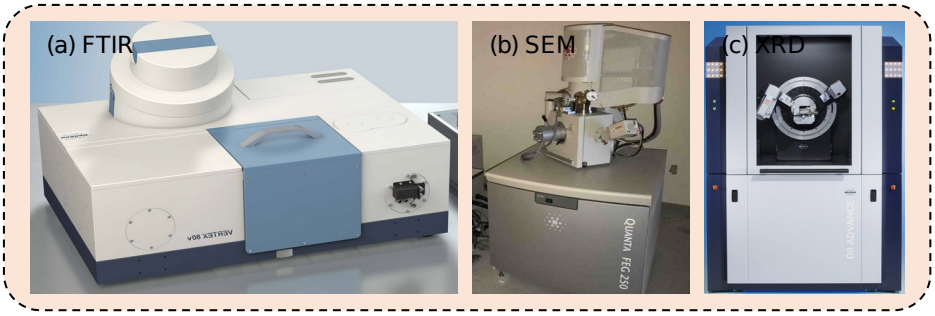


**Figure 4** Experimental setup for the characterization of physicochemical properties.

(a) VERTEX 80v FTIR; (b) FEI Quanta TM 250 SEM; (c) D8 Advance XRD.

### 2.4 Experiment design

Factors affecting wettability of coal include physical and chemical properties of coal (mainly surface functional groups and mineral components) and ~~external~~ environmental ~~factors~~ conditions (~~such as~~ temperature and pressure). In the process of $CO_2$ injection into water-bearing coal seams for storage or methane displacement, high pressure or chemical reaction may impact the physical and chemical structure of coal surfaces, and thereby affect the wettability of coal.

In this study, wettability changes over time were measured ~~when~~ following coal ~~was~~ expos~~ed~~ure to low pressure (gaseous) and high pressure (supercritical) $CO_2$. Due to the poor water solubility of $CO_2$ under low pressure conditions, ~~the~~ its impact on the physical and chemical properties of the coal surface may be not significant, but under high pressure conditions, $CO_2$ dissolved in water will form an acidic solution, which may have a greater impact on the physical and chemical properties of coal surface. $N_2$ (the most chemically stable of the known diatomic molecules) is much less soluble in water, so the chemical reaction between its aqueous solution and coal is negligible. Therefore, we also measured the wettability variation of coal surfaces exposed to $N_2$ under the same experimental conditions, in order to determine the influence of coal reaction with $CO_2$ aqueous solutions on wettability. The specific experimental conditions are shown in **Table 2**.

**Table 2** Experimental conditions.

| Type | Critical point | Gas~~eous~~ phase | Supercritical phase |
|---|---|---|---|
| **$N_2$** | $P$=34.0 bar, $T$=−147.0°C | ~23°C, 20 bar | 45°C, 120 bar |
| **$CO_2$** | $P$=73.8 bar, $T$=31.2°C | ~23°C, 20 bar | 45°C, 120 bar |

## 3 Results

### 3.1 Coal-$N_2$-$H_2O$ competitive wetting

**Figure 5** gives time-dependent dynamic contact angles for $N_2$-$H_2O$-coal systems (values are given in **Table A.3** and **Table A.4**). For gaseous $N_2$ ($P$=20 bar, $T$=25°C), the average advanced ($\theta_{adv}$) and receding ($\theta_{rec}$) contact angles are 28~32° and 22~23.5°, respectively, indicating strong water-wetting. The variation of contact angles was less than 5°, indicating that time-dependent wettability of coal in gaseous $N_2$-$H_2O$-coal systems is stable under low pressure. For $scN_2$ ($P$=120 bar, $T$=45°C), the $\theta_{adv}$ (24.5~28.5°) and $\theta_{rec}$ (18.5~21.5°), also changed very slightly and were close to values under low pressure due to slight variation of density (Zhu et al., 2019). The static contact angles for gaseous $N_2$ and $scN_2$ are 23~25° and 22~24°, respectively, which ~~are~~ follow similar trends as dynamic contact angles, as shown in **Figure 6**.

Gas or supercritical $N_2$ is ~~nearly~~ relatively insoluble in water and cannot form acid

solution that react with coal under the current experimental condition. The calculated solubility of $N_2$ in water is ~$9.76\times10^{-5}$ mol/mol at 120 bar and 45°C (Battino et al., 1984). Therefore, the only factor that may affect wettability is the high pressure. The applied high pressure is expected to change pore structure of coal (such as pore compaction, pore expansion) or generate ~~hydro-~~fractures (Jia et al., 2022; Wang et al., 2022). However, based on the results of time-dependent dynamic and static contact angles, these physical changes of coal surface caused by high pressure $N_2$ did not have a significant effect on wettability.

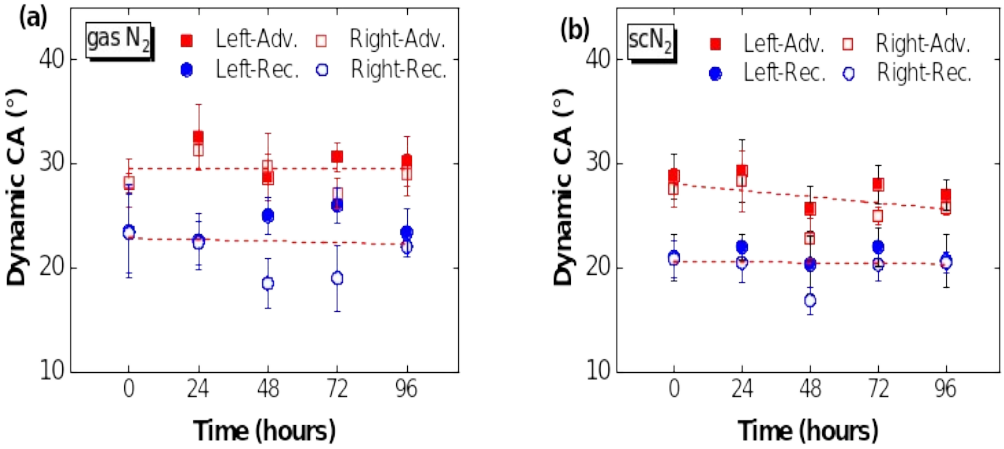


**Figure 5** Time-dependent dynamic CAs with $N_2$ treatment. (a) Dynamic contact angle under gaseous $N_2$ ($P$=20 bar, $T$=25°C), (b) Dynamic contact angle under $scN_2$ ($P$=120 bar, $T$=45°C). "Left-Adv" and "Right-Adv" refer to the advancing contact angles measured on the left and the right side of bubbles, respectively.

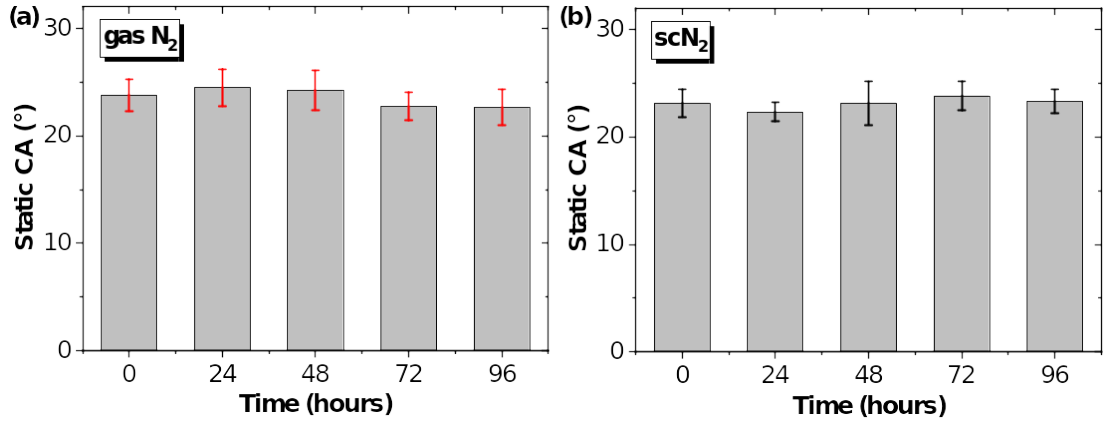


**Figure 6** Time-dependent static CAs. (a) Static contact angle under gaseous $N_2$ ($P$=20 bar, $T$=25°C), (b) Static contact angle under $scN_2$ ($P$=120 bar, $T$=45°C).

### 3.2 Coal-$CO_2$-$H_2O$ competitive wetting

~~Figure 7 gives~~ The time-~~dependent~~ dependence of dynamic contact angles (CAs) exposed to gas and supercritical $CO_2$-$H_2O$ systems~~, respectively~~ are presented in **Figure 7**. For ~~gas $CO_2$~~gaseous $CO_2$, the average advancing contact angles ($\theta_{adv}$) varied from 34.1° to 45.7°. The dynamic CA at 0 hour was the highest (with an average value

of 45.7°), ~~which makes~~followed by $\theta_{adv}$ ~~show a downward trend~~decreasing with time. However, dynamic advancing CAs for ~~gas $CO_2$~~gaseous $CO_2$ varied little (~5.3°) from 24 hours to 96 hours, and average receding contact angles ($\theta_{rec}$) changed ~~more~~ slightly (19° to 24°). In contrast, for $scCO_2$, both $\theta_{adv}$ and $\theta_{rec}$ show obvious increas~~ing trends~~es over time, especially for the $\theta_{rec}$ which increased from 35° (0 hour) to 50° (96 hours). The $\theta_{adv}$ with $scCO_2$ changed from water-wet to intermediate-wet.

We also measured the time-~~dependent~~ dependence of static contact angles (CA) as shown in **Figure 8**. Average static CAs in ~~gas $CO_2$~~gaseous $CO_2$ fluctuated between 22° and 26°, while those in $scCO_2$ increased dramatically from 35° (0 hour) to 56° (96 hours). Additionally, the static CA in $scCO_2$ tends to be stable after 48 hours of reaction. The greater CA after $scCO_2$ treatment is ~~attributes~~ attributed to decrease in pH and more ~~intense~~ extensive mineral reactions, as will be discussed in section 4.1. The increases ~~of~~ in CA with decreasing pH in carbonate solution is consistent with a previous report (Chaturvedi et al., 2009) (4<~~PH~~pH<7) as shown in **Figure 9**.

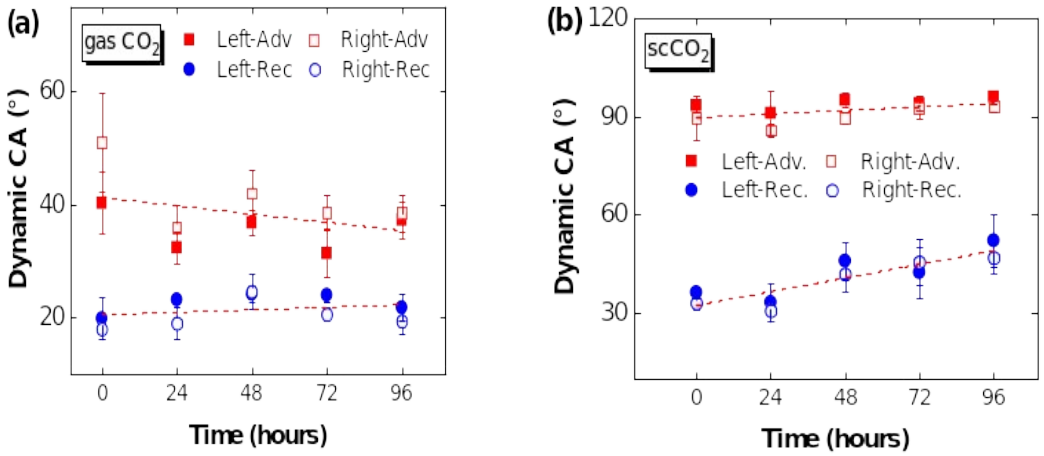


**Figure 7** Time-dependent dynamic contact angles with $CO_2$ treatment. (a) Dynamic CA under ~~gas $CO_2$~~gaseous $CO_2$ ($P$=20 bar, $T$=25°C), (b) Dynamic CA under $scCO_2$ ($P$=120 bar, $T$=45°C).

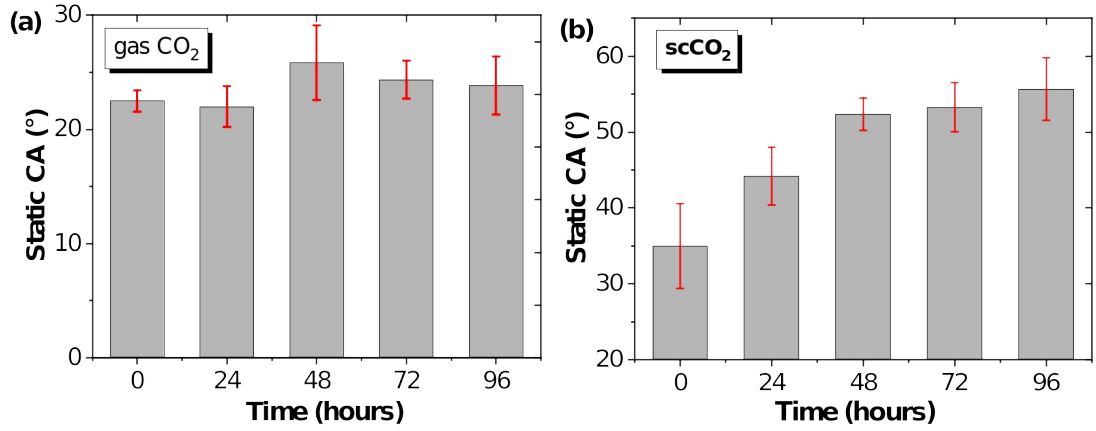


**Figure 8** Time-dependent static contact angles. (a) Static CA under ~~gas $CO_2$~~gaseous $CO_2$ ($P$=20 bar, $T$=25°C), (b) Static CA under $scCO_2$ ($P$=120 bar, $T$=45°C).

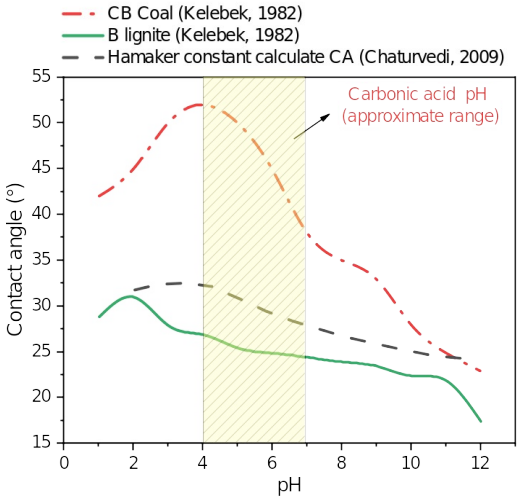


**Figure 9** Experimental and calculated contact angles of CB coal and B lignite coal samples with pH (Kelebek, 1982), and calculated CA (Chaturvedi et al., 2009). pH depends on solute concentration and ionization equilibrium constant in the solution, and the pH of carbonic acid usually ranges from 4–7 (MacInnes and Belcher, 1933).

# 4 Discussion

## 4.1 Coal surface micromorphology

The coal-sc$CO_2$-$H_2O$ interaction affects wettability ~~by~~ through three main physicochemical mechanisms ~~from the perspective of physicochemical property as~~ shown in **Figure 10a**. Surface roughness has a potential effect on specific surface area and surface free energy, which consequently affects wettability (Wei et al., 2022). After sc$CO_2$ treatment, the appearance of corrosion pores, connecting partially isolated pores, fracture extension, and edge warping in **Figure 10b** changed surface roughness and pore structure, which ~~results~~ resulted from chemical reactions between minerals and the weakly acidic solution. $CO_2$ dissolved in water produces$H^{+¿¿}$ and $HCO_3^{-¿¿}$ ions in acidic systems (Lerman and Mackenzie, 2018) as shown in Eq.(1). These ions, along with $H_2O$ and $CO_2$ molecules, altered the mineral composition (mineral composition of raw coal as shown in **Table A. 1**) through reaction Eqs.(2)–(5) (Ao et al., 2017; Labus and Bujok, 2011). The dissolution of the minerals, especially hydrophilic clay and carbonate minerals, has been also reported in previous studies (Fatah et al., 2021b; Lu et al., 2021). The brownish-yellow substance in **Figure 10b** ~~was~~ is FeO(OH), which was produced by Fe oxidation of ferrous carbonate to FeO(OH) in the carbonic acid solution.

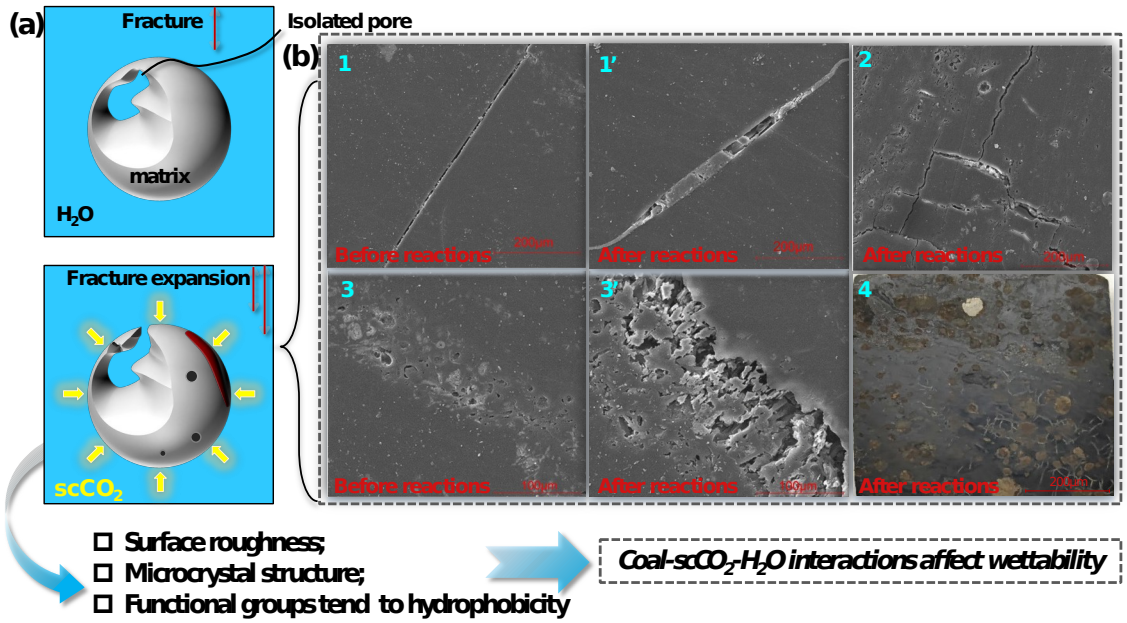


**Figure 10** The changes of physicochemical property exposed to $scCO_2$. (a) Schematic diagram of three mechanisms for the effect of coal-$scCO_2$-$H_2O$ interactions on wettability. (b) Coal surface micrographs: (1–1') fracture extension before and after reactions with $scCO_2$; (2) edge warping after reactions with $scCO_2$; (3–3') corrosion pores and connection of isolated pores before and after reactions with $scCO_2$; (4) brownish-yellow FeO(OH) after reactions with $scCO_2$. Note: Some of the micrographs in Figure 10 (b) ~~were used to~~served as the basis for drawing the mechanism schematic in our recently published paper (S. Liu et al., 2023).

$$CO_{2(aq)} + H_2O \Leftrightarrow H^{+} + HCO_3^{-} \quad (1)$$

$$\underset{\text{Calcite}}{CaCO_3} + CO_2(aq) + H_2O \Leftrightarrow Ca^{2+} + 2\,HCO_3^{-} \quad (2)$$

$$Al_2Si_2O_5 \quad (3)$$

$$\underset{Dolomite}{CaMg(CO_3)_2} + 2\,H^{+} \Leftrightarrow Ca^{2+} + Mg^{2+} + 2HCO_3^{-} \quad (4)$$

$$K_{0.6}Mg_{0.25}Al_{2.3}Si_{3.5}O_{10} \quad 0.6\,KAl_3Si_3O_{10} \quad (5)$$

Additionally, adsorption sites of coal surface increased after reaction with $scCO_2$ since surface fractures are developed and connected (Chen et al., 2019). ~~Denser~~ The higher concentration of $CO_2$ molecules convert some $H_2O$-occupied sites to $CO_2$-occupied sites (Yu et al., 2022), partially displacing the adsorbed water and transforming the coal surface into a heterogeneous surface comprising of solid and $CO_2$-occupied~~gas~~ pockets (Sun et al., 2022). The adsorption and interaction energy of $CO_2$ molecules are enhanced in the supercritical state on the coal surface ~~are enhanced~~ (Liu et al., 2010), which causes $CO_2$ to ~~reside and~~ accumulate as a thin film at the solid/liquid interface (Iglauer et al., 2012; Xu et al., 2023). The chemical reactions of

minerals resulted in a rougher coal surface which promotes $CO_2$ adsorption ~~on the surface~~, and this interfacial behavior favors $CO_2$-wetting (Zhou et al., 2022).

Contact angle hysteresis, or the difference between $\theta_{adv}$ and $\theta_{rec}$ denoted by $\Delta\theta$, results from variation of surface roughness ~~or,~~ chemical inhomogeneity, and pinning effects (Cai and Song, 2021; Kulinich and Farzaneh, 2009). The average $\Delta\theta$s of coal for gaseous $N_2$ and $scN_2$ treatment were 7.0° and 6.3° as in **Figure 11a**, respectively, which were obviously smaller than those of coal for $CO_2$ treatment as shown in **Figure 11b**. The average $\Delta\theta$ of coal was 16.8° for ~~gas $CO_2$~~gaseous $CO_2$ treatment, while it increased to 52.6° for $scCO_2$ treatment. The ~~molar~~ mole fraction of $CO_2$ solubility in water ranges from $0.695\times10^{-3}$ in the gaseous state (T=20°C, P=1 bar) to $2.51\times10^{-3}$ in the supercritical state (T=50°C, P=85.1 bar) (Sabirzyanov et al., 2002). Differences in $\Delta\theta$ indicate that chemical reactions resulted in greater surface inhomogeneity of coal after reaction with $scCO_2$.

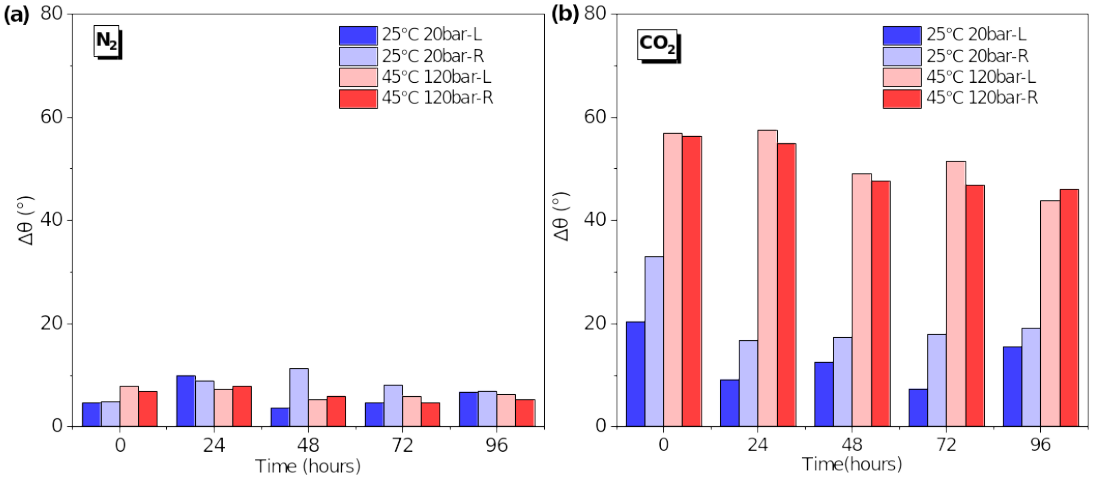


**Figure 11** Contact angle hysteresis denoted by $\Delta\theta$ with time for $CO_2$ and $N_2$ treatment under different pressures and temperatures, respectively. "L" and "R" refer to CA measurements on the left and the right side of bubbles, respectively.

### 4.2 FTIR functional groups

Surface roughness mainly reflects physical structure, and the influence of surface chemistry (functional groups, crystallite structure) on wettability also needs to be further discussed. The FTIR spectra of coal are usually divided into four absorption bands (Lu et al., 2021), i.e., hydroxyl groups (3700–3200 $cm^{-1}$), aliphatic hydrocarbons (3000–2800 $cm^{-1}$), oxygen-containing groups (1800–1000 $cm^{-1}$), and aromatic hydrocarbons (900–700 $cm^{-1}$). The assignment of functional groups in each absorption band is shown in **Figure 12a**. **Figure 12b** gives FTIR spectra of raw coal, and coal with $H_2O$ treated by $scN_2$ or $scCO_2$ at $T$=45°C and $P$=90 bar after 96 hours, respectively. Absorption peaks of three group experiments had similar peak shape but different peak intensity and area, indicating that the content of functional groups changed but types of functional group and macromolecular structure remained basically similar (Shang et al., 2021). Due to the influence of algorithms, samples, and

setups, absorption peaks in the same band could still be shifted and overlapped (Wang et al., 2017). Previous studies disputed assignment of different peak positions to the same functional group (Yan et al., 2020), so we used integral areas of sub-peaks rather than peak intensity to determine types and content of functional groups. The fitted curves were decomposed into sub-peaks controlled by Gaussian or Lorentz algorithms with the correlation coefficient $R^2 > 0.98$.

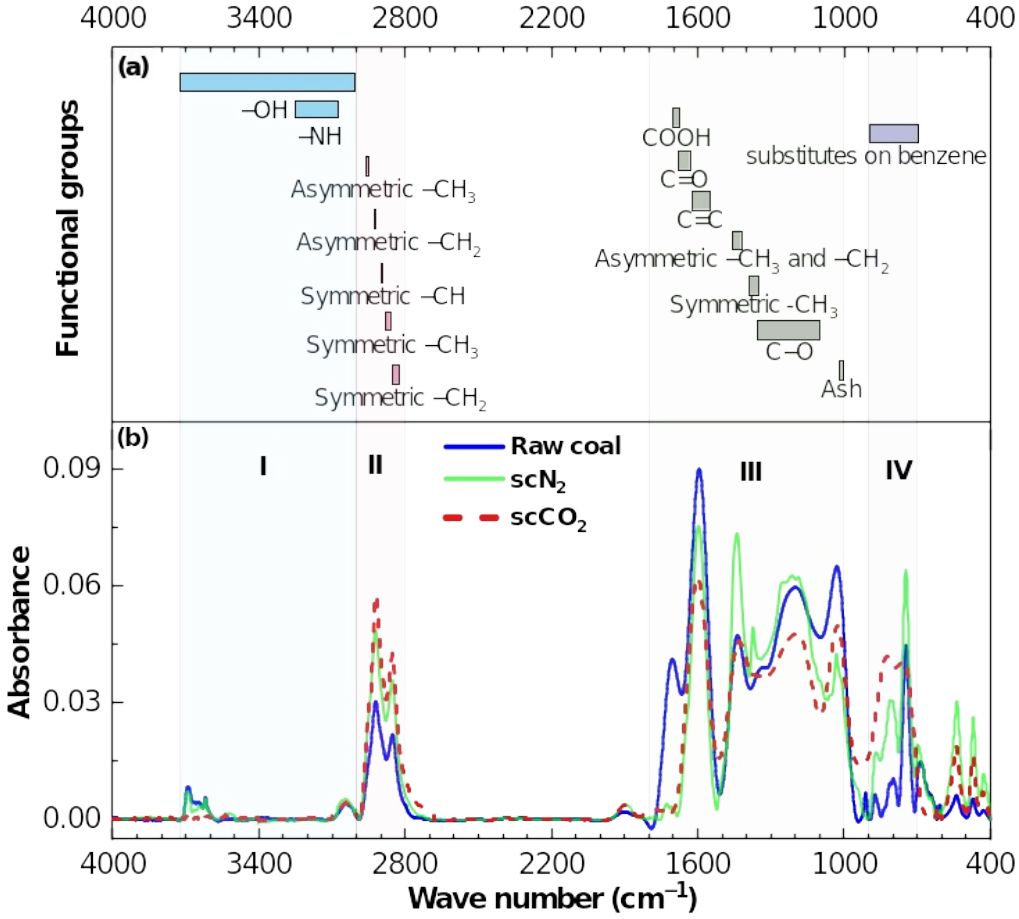


**Figure 12** The FTIR spectra and assignment of functional groups. (a) Assignment of functional groups of coal surface in the range of 4000–400 $cm^{-1}$. (b) The FTIR spectra of raw coal, $scN_2$, and $scCO_2$ were divided into four absorption bands: Ⅰ—Hydroxyl groups, Ⅱ—Aliphatic hydrocarbons, Ⅲ—Oxygen-containing groups, Ⅳ—Aromatic hydrocarbons.

(1) Hydroxyl functional groups

The absorption peaks in the range of 3700–3200 $cm^{-1}$ ~~were~~ are mainly generated by stretching vibration of –OH, which is the main functional group for the formation of hydrogen bonds. As shown in **Figure 13**, absorption peaks appeared in the range of 3650–3400 $cm^{-1}$, and main types of hydroxyl groups are OH–π, OH–OH, and free–OH.

The peak shape of coal for $scCO_2$ treatment was different from that of raw coal and coal for $scN_2$ treatment in **Figure 13**, and all of the sub-peak intensities of coal for

$scCO_2$ treatment were below 0.001. The integral areas of sub-peaks of hydroxyl groups for coal with $H_2O$ treated by $scCO_2$, $scN_2$ and raw coal were 0.125, 0.424, and 0.549, respectively. The reduction of hydroxyl groups decreases the number of hydrogen bonds between $H_2O$ molecules and C atoms of coal (Besford et al., 2020), whereas intermolecular forces (~~Van~~ van der Waals) between $CO_2$ molecules and coal C atoms become prominent. Thus the adsorption potential of $CO_2$ on coal increases significantly ("Surface physical properties and its effects on the wetting behaviors of respirable coal mine dust," 2013). Water films on the surface were ~~gradually~~ displaced by $CO_2$ dissolved in water, and water-wet surfaces changed to be intermediate-wet or $CO_2$-wet.

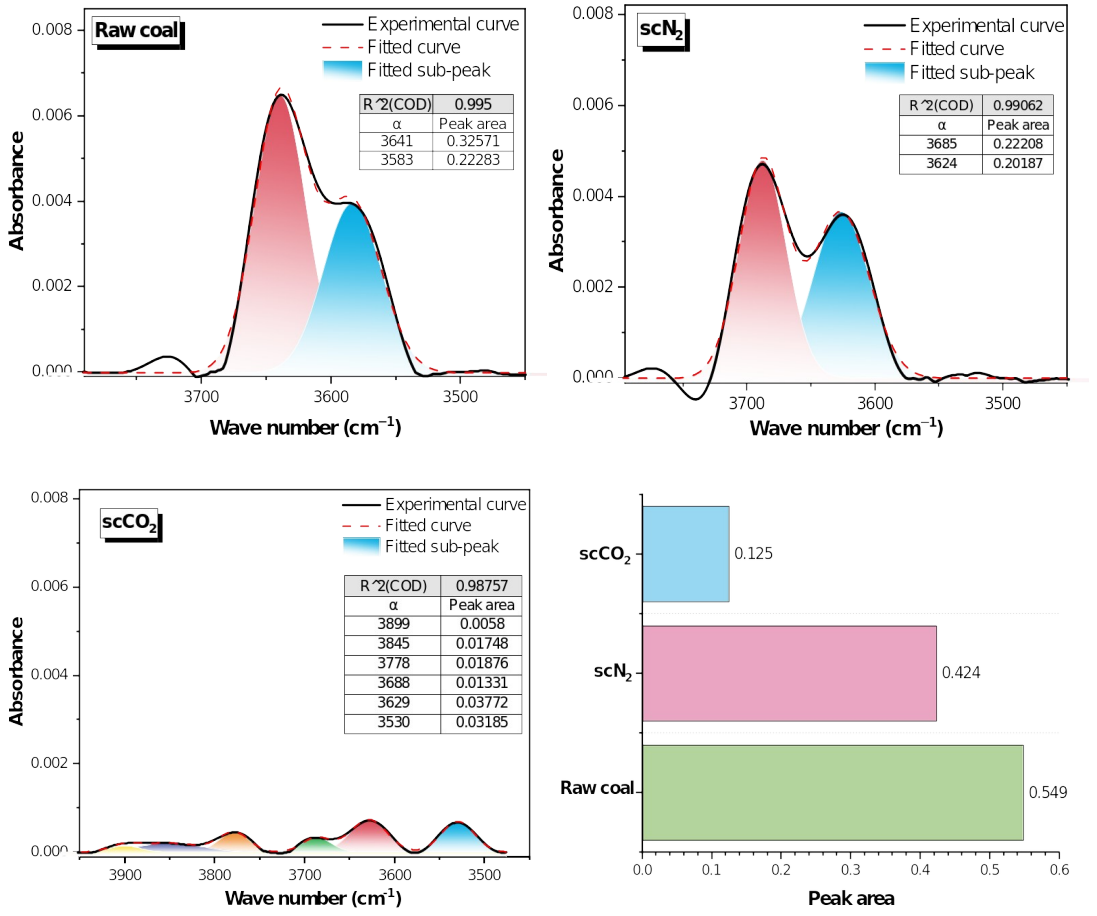


**Figure 13** Curve-fitting of FTIR spectra in the range of 3700–3200 $cm^{-1}$. α in the tables represents ~~peak~~ wave number, $cm^{-1}$. Peak areas from the different conditions are compared in the lower right bar graph.

(2) Aliphatic hydrocarbons

In **Figure 14**, the absorption peaks in the range of 3000–2800 $cm^{-1}$ were mainly assigned to asymmetric vibrations of $-CH_2$ and $-CH_3$, and symmetric vibrations of $-CH_2$ and $-CH_3$. The peak positions of the above functional groups are located around 2943 $cm^{-1}$, 2923 $cm^{-1}$, 2901 $cm^{-1}$ and 2852 $cm^{-1}$, respectively.

The integral areas of sub-peaks of aliphatic hydrocarbons for coal with $H_2O$ treated

by $scCO_2$, $scN_2$ and raw coal were 7.04, 4.08, 3.97, respectively. The increase of aliphatic structure results from the alkylation of hydrocarbons under acidic conditions and implies an increase of the C atom ratio (Ni et al., 2019; Zhang et al., 2023). For $scCO_2$-$H_2O$ treatment, the peak areas of the sub-peaks corresponding to $-CH_3$ and $-CH_2$ increased from 1.38 and 2.27 to 2.50 and 4.20, with $-CH_2$ having greater relative increase. ~~Previous~~ A previous study (Guanhua et al., 2019) reported that wettability is positively correlated with the percentage area of $-CH_3$ and negatively correlated with $-CH_2$. This suggests that ~~the changes of aliphatic hydrocarbons are detrimental to water-wetting, and~~ carbon content increased after the chemical reactions, and that increases in surface coverage with aliphatic hydrocarbons are detrimental to water-wetting.

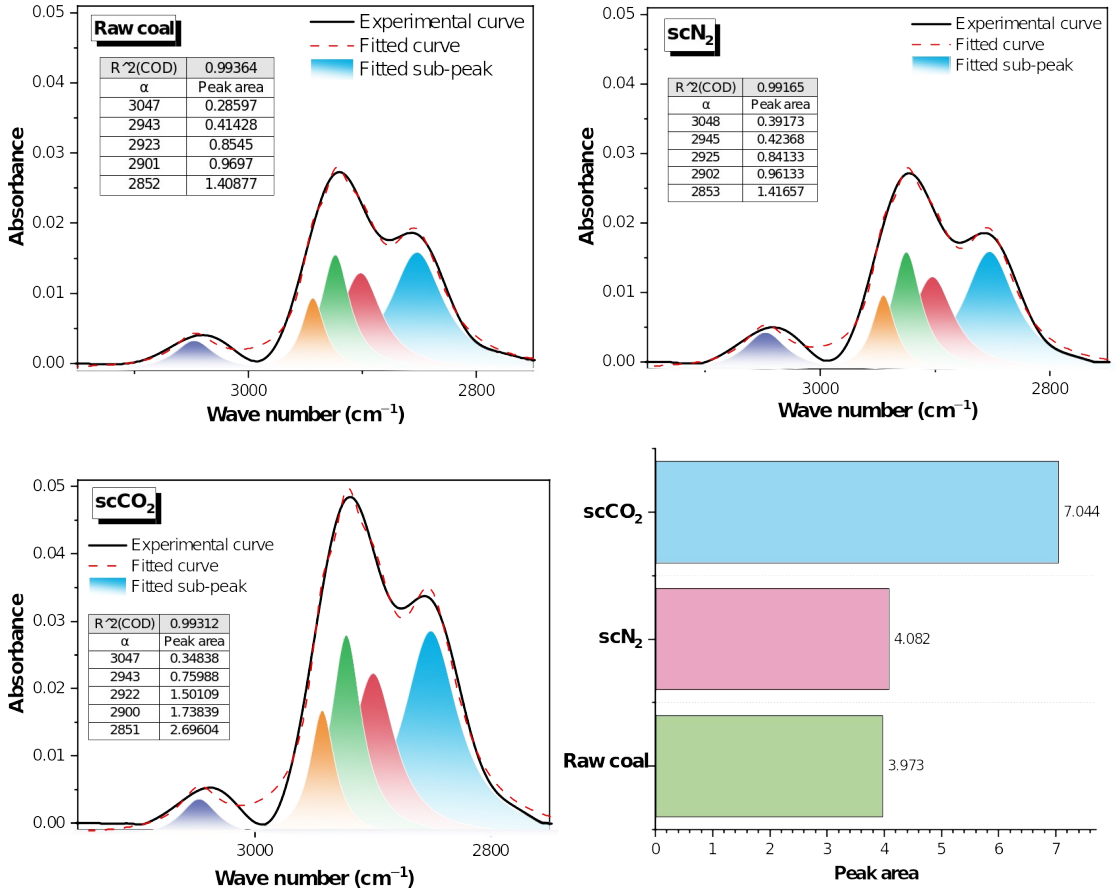


**Figure 14** Curve-fitting of FTIR spectra in the range of 3000–2800 $cm^{-1}$. α in the tables represent peak wave number, $cm^{-1}$. Peak areas from the different conditions are compared in the lower right bar graph.

(3) Oxygen-containing functional groups

As shown in **Figure 15**, the absorption peaks of oxygen-containing functional groups were mainly in the range of 1800-1000 $cm^{-1}$. The functional groups were assigned to COOH, aromatic nucleus C=C, symmetric $-CH_3$, C–O, C–O–C, which located near 1705 $cm^{-1}$, 1595 $cm^{-1}$, 1362 $cm^{-1}$, 1206 $cm^{-1}$, and 1068 $cm^{-1}$, respectively.

The integral areas of the sub-peaks of oxygen-containing functional groups for raw

coal, ~~and~~ coal with $H_2O$ treated by sc$N_2$~~$CO_2$~~, and coal with $H_2O$ treated by sc $CO_2$~~$N_2$~~ were 38.28~~20.33~~, 34.52~~ 34.52~~, and 20.33~~ 38.28~~, respectively. The decrease of oxygen-containing functional groups after sc$CO_2$ treatment ~~is related to~~reflects their shedding or dissociation on the surface (Boehm, 1989). Oxygen-containing functional groups, including many polar components ~~(Crawford et al., 1994)~~ (Crawford et al., 1994), especially carboxyl groups, enhance interaction forces with polar molecules such as $H_2O$ and are much stronger than the intermolecular forces (induced force and dispersion force) between $CO_2$ and oxygen-containing functional groups (Siemons et al., 2006). Therefore, it is difficult for $CO_2$ to displace $H_2O$ molecules adsorbed directly on oxygen-containing functional groups at room-temperature and ambient-pressure (Gensterblum et al., 2014). Wu et al. similarly reported ~~the~~ that reduction of oxygen-containing functional groups leads to weaker water-wetting as reflected in the shrinkage of precursor films and lower surface free energy (Wu et al., 2017). Shedding of polar oxygen-containing functional groups (especially carboxyl groups) after reactions with sc$CO_2$ significantly weakened water-wetting.

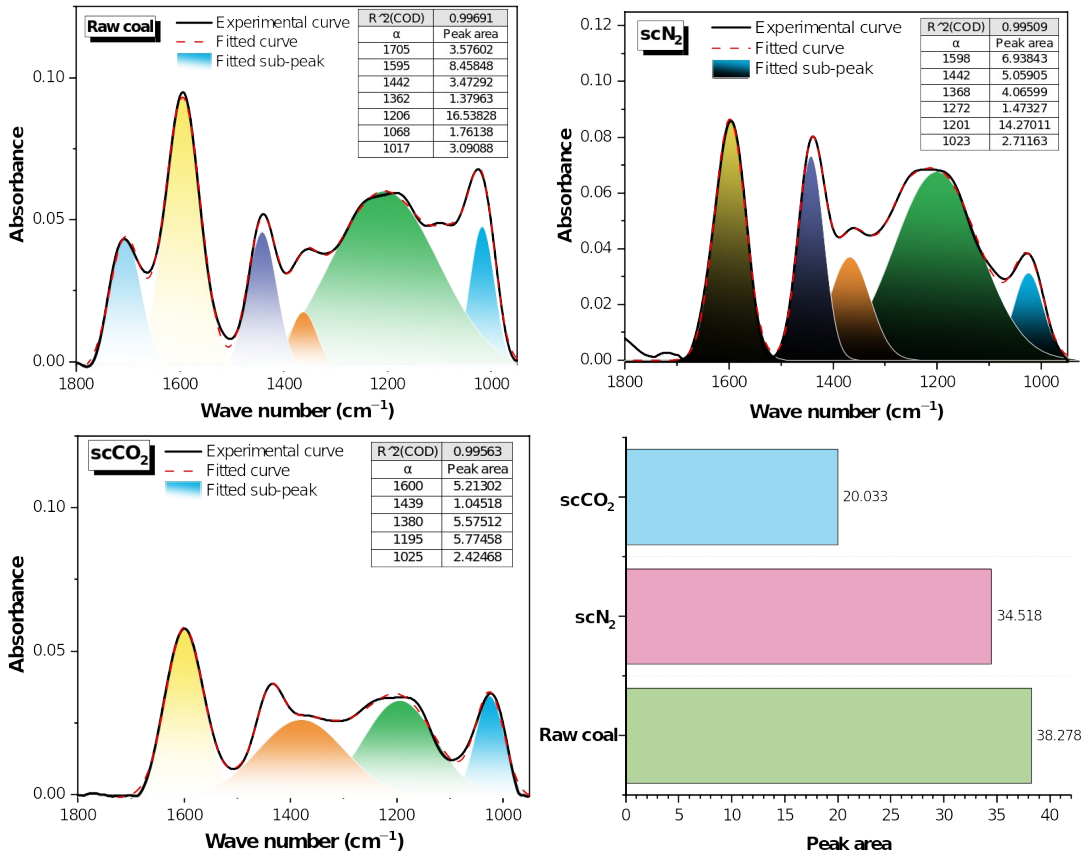


**Figure 15** Curve-fitting of FTIR spectra in the range of 1800–1000 $cm^{-1}$. α in the tables represent peak wave number, $cm^{-1}$. Peak areas from the different conditions are compared in the lower right bar graph.

(4) Aromatic hydrocarbons

The adsorption peaks of waveband 900–600 $cm^{-1}$ in **Figure 16** mainly were

assigned to the bending vibrations of substituted benzene rings. Compared with aliphatic hydrocarbons, most of aromatic hydrocarbons are also insoluble in water, but the aromatic system is more stable.

The integral areas of the sub-peaks of aromatic hydrocarbons for raw coal, coal treated by ~~scCO$_2$,~~ scN$_2$~~,~~ and by scCO$_2$ ~~and raw coal~~ were 1.79~~7.11~~, 2.47, and 7.11~~1.79~~, respectively. After scCO$_2$ treatment, the peak intensities and peak areas of two sub-peaks near 853 cm$^{-1}$, 806 cm$^{-1}$ increased significantly, which was attributed to the increase of aromatic structure content (Wang et al., 2023) (main contribution), $CO_3^{2-}$ ions, and silica (Fatah et al., 2021b; Reig et al., 2002) .

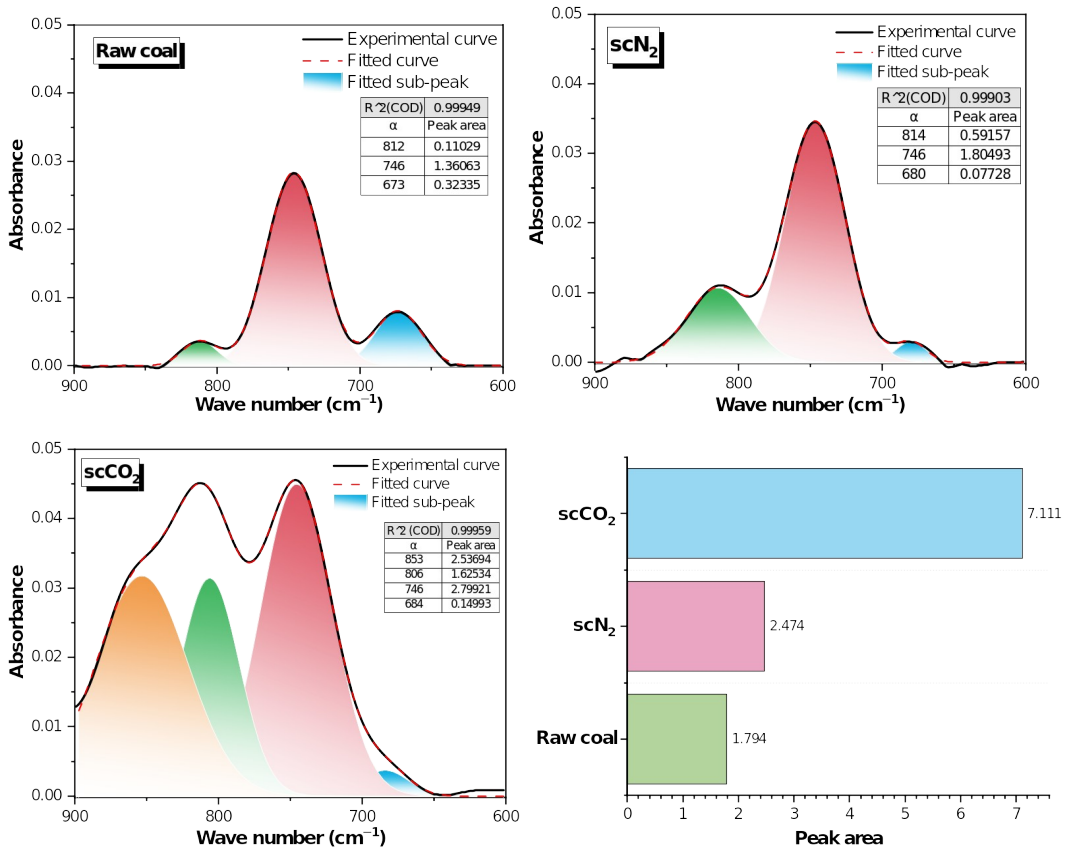


**Figure 16** Curve-fitting of FTIR spectra in the range of 900–700 cm$^{-1}$. α in the tables represent peak wave number, cm$^{-1}$. Peak areas from the different conditions are compared in the lower right bar graph.

Infrared structural parameters used to characterize chemical structure are defined and reported in **Table 3**. We obtain the following conclusions:

1. Aromaticity ($I$) represents the abundance of aromatic hydrocarbons relative to aliphatic hydrocarbons. The increase of aromaticity implies the gradual decrease of coal defects and disorder.

2. $CH_2/CH_3$ represents the length of aliphatic chain and branching degree. The increase of $CH_2/CH_3$ ~~means~~ indicate more aliphatic chain and less branched chains.

3. The degree of aromatic ring condensation ($DOC$) represents the ratio of aromatic C atoms to aromatic clusters and aromatic ring condensation. The increase of $I$, $CH_2$/

$CH_3$, and $DOC$ after $scCO_2$ treatment indicates more stable structure and elevated coal rank. ~~Eventually graphitization~~ Graphitization and hydrophobicity are eventually enhanced, ~~which~~ as will be ~~further~~ discussed in 4.3 section.

**Table 3** Infrared structure parameters.

| Structure parameter | Formula | Experimental group | | |
|---|---|---|---|---|
| | | $scCO_2$ | $scN_2$ | Raw coal |
| Aromaticity | $I=\frac{A_{900\sim700}}{A_{3000\sim2800}}$ | 1.279 | 0.775 | 0.563 |
| Degree of aromatic ring condensation | $DOC=\frac{A_{CH_2}+A_{CH_3}}{A_{C=C}}=\frac{A_{900\sim700}}{A_{1605\ 1595}}$ | 1.368 | 0.356 | 0.212 |
| Length of aliphatic hydrocarbon chain | $A(CH_2)/A(CH_3)=\frac{A_{2920+2850}}{A_{2950+2870}}$ | 1.68 | 1.630 | 1.637 |

The overall impact of different treatments on surface chemistry is quantified by the average relative change of the absorption peak area ($\Delta'$), given by

$$\Delta'=\frac{\sum_{}^{}\left|A_{}-A_{}\right|}{A_{}} \quad (6)$$

~~In conclusion~~From this metric, changes in functional group content from $scN_2$-$H_2O$ treatment were small relative to the original raw coal, ~~and the relative change of the absorption peak area ($\Delta'A$ that ) wa~~is only 0.15 times that for the $scCO_2$-$H_2O$ treatment~~.~~. Such minor changes in surface chemistry imparted by exposure to $scN_2$, are consistent with small changes in measured contact angles. ~~It is difficult for $scN_2$ to alter surface chemistry, which corresponds to the results of contact angle measurement.~~

~~It is difficult for $scN_2$ to alter surface chemistry, which corresponds to the results of contact angle measurement.~~ After $scCO_2$-$H_2O$ treatment, the density of hydrophilic functional groups (hydroxyl and other polar oxygen-containing functional groups (Zhao et al., 2023)) decreased, while the hydrophobic functional groups (aromatic and aliphatic hydrocarbons (Xu et al., 2017)) increased. This tendency towards hydrophobicity results from three aspects: (1) the shedding of polar oxygen-containing functional groups, (2) the reduction of hydrogen bonds, (3) elevated coal rank and the increased percentage of surface hydrocarbons. Fewer sites of polar oxygen-containing functional groups were available for $H_2O$ directly adsorbing (dark color in **Figure 17** (b)). The intermolecular force (hydrogen bonds between $H_2O$) and long-distance attractions weakened so that $H_2O$ in multilayer adsorption (light color) was displaced or washed away by $CO_2$. Coal surfaces with a higher percentage of hydrocarbons and a tendency to be graphitized are more hydrophobic and more capable of $CO_2$ adsorption.

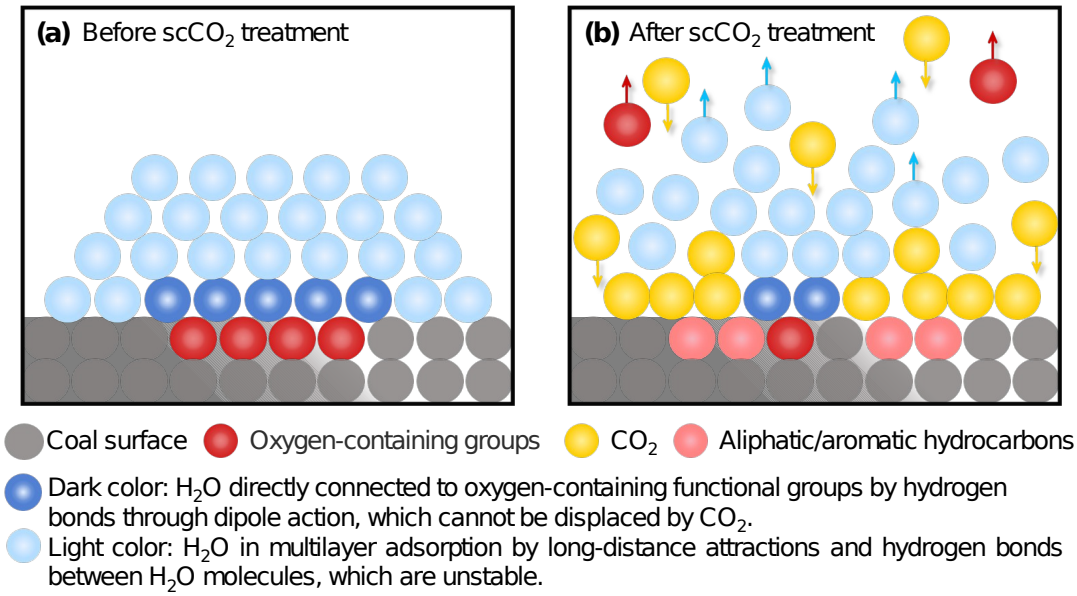


**Figure 17** Schematic diagram of the effect of $CO_2$ adsorption and functional group alterations on wettability.

### 4.3 Coal crystallite structure

XRD patterns of coal generally have two diffraction peaks (002- and 100-peak) corresponding to diffraction angles ($2\theta$) ~26° and 44°, respectively. The asymmetry of diffraction peak (raw curve in **Figure 18**) is caused by the γ-band related to saturated structures like aliphatic chains or aliphatic rings (Kamble et al., 2022). The 002-peak was distinct while the 100-peak was not, as shown in **Figure 18**, indicating that the main crystalline phase is carbon.

In general, the intensity of the diffraction peak decreased after $scCO_2$ treatment, indicating that mineral content decreased, especially calcite (club label near $2\theta$~30° in **Figure 18**), and only the diffraction peak of quartz (heart label) was still clearly present. As shown in **Figure 18**, residual analysis showed that conventional residuals at the peak position of calcite deviated clearly from mode-fitting values of cumulative curve. The diffraction peak of calcite was the reason for coefficient of determination $R^2$<0.90 in raw coal and $scN_2$ treatment. A previous study eliminated this strong peak in coal by acid leaching (Yan et al., 2020), ~~which corresponds to~~causing the decomposition of calcite in carbonic acid as described by Eqs. (2).

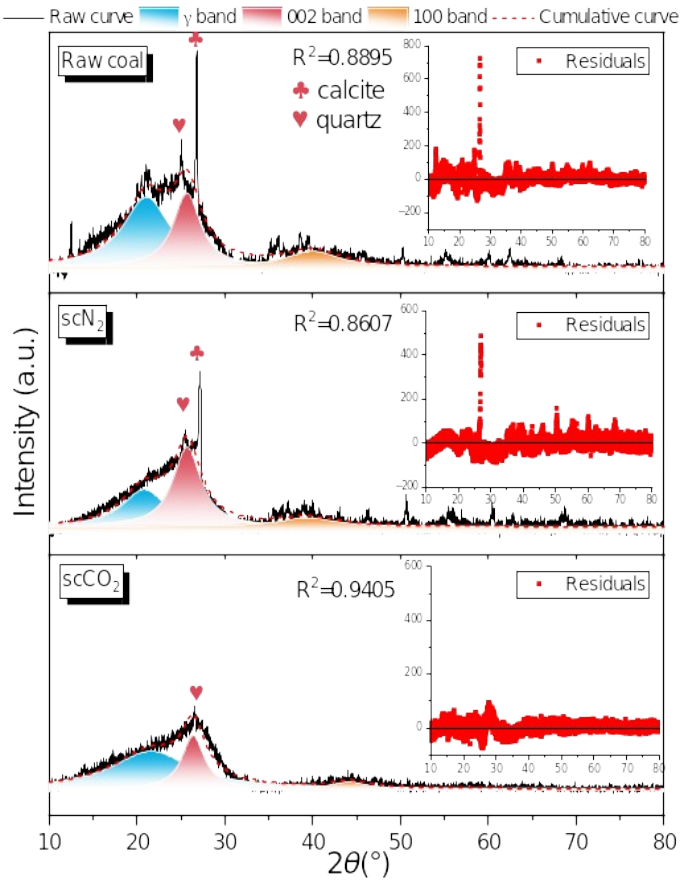


**Figure 18** Curve-fitting of XRD patterns and residual analysis. The mineral ~~labels~~ labeling ~~were~~ was ~~conducted according to~~accomplished through ~~comparing~~ comparisons with standard cards in Jade and with previous work (Tian et al., 2017; Yan et al., 2020).

Crystallite structure parameters in **Table 4** were calculated with the ~~Bragges~~ Bragg's and Scherrer's formulae (7)–(11) (Matlala et al., 2021): aromatic interlayer spacing $d_{002}$, crystallite diameter $L_a$, crystallite height $L_c$, the number of aromatic stacking layers $N$, and coalification degree $D$. Full width at half maximums (FWHM) and peak mean centers of 002- and 100-peak used to calculate crystallite parameters were obtained from the fitting results shown in **Table A.2**.

The $d_{002}$ for raw coal, $scN_2$ treatment, and $scCO_2$ treatment were 3.46 Å, 3.46 Å, 3.37 Å, respectively, and the reduction of interlayer spacing implied closer arrangement of aromatic layer structure. For $scCO_2$ treatment, the diffraction angle of 002-peak was 26.4° and close to that of pure graphite (26.6°). $L_a$, $L_c$, and $N$ both increased, indicating the degree of molecular polymerization and the size of carbon crystalline developed (Sonibare et al., 2010). The $D$ for raw coal, $scN_2$ treatment, and $scCO_2$ treatment were 82.3%, 82.6%, and 97.1%, respectively. From the XRD patten of the $scCO_2$ treated coal, we find that inorganic mineral abundance reduced, and carbon crystallites tended to graphite-like structure: the crystallite growth and the higher degree of long-range ordering in aromatic carbon (Zhang et al., 2021). These

changes to crystallite structure are usually detrimental for water-wetting because of the higher carbon content and the lower negative surface charge after structure development (Fuerstenau et al., 1988). Moreover, crystallite development usually is associated with elevated coal rank, which is positively correlated with contact angle (Shojai Kaveh et al., 2012; Yan et al., 2015).

$$d_{002}=\frac{\lambda}{2\sin\theta_{002}} \quad (7)$$

$$L_a=\frac{K_1\lambda}{\beta_{(100)}\cos\theta_{(100)}} \quad (8)$$

$$L_c=\frac{K_2\lambda}{\beta_{(002)}\cos\theta_{(002)}} \quad (9)$$

$$N=\frac{L_c}{d_{002}}+1 \quad (10)$$

$$D=\frac{d\square_{CE}-d_{002}}{d\square_{CE}-d\square_{GR}}\times 100\% \quad (11)$$

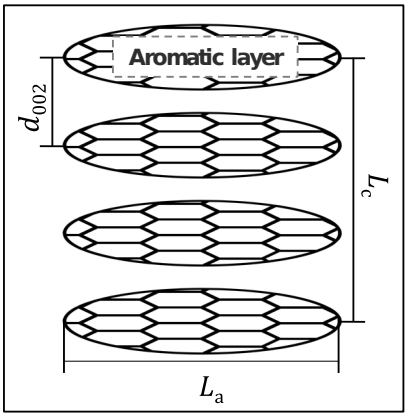


where λ is the X-ray wavelength, the copper target is taken as 1.54056 Å; $\theta_{(002)}$, $\theta_{(100)}$ are the Bragg angles of the 002 and 100 diffraction peaks, respectively, (°); $\beta_{(002)}$, $\beta_{(100)}$ are the half-height widths of the 002 and 100 diffraction peaks, respectively, (rad); $K_1$, $K_2$ are Debye-Scherrer constants and crystallite shape factors. $K_1$, $K_2$ are taken as 1.84, 0.94, respectively. $d\square_{CE}$ and $d\square_{GR}$ are cellulose of $d_{002}$=¿3.975 Å and graphite of $d_{002}$=¿3.354 Å, respectively.

**Table 4** Crystallite structure parameters.

| Coal sample | $d_{002}$/ Å nm | $L_a$/ Å | $L_c$/ Å | $N$ | $D$/% |
|---|---|---|---|---|---|
| **Raw coal** | 3.46 | 25.69 | 23.80 | 7.87 | 82.28% |
| **$N_2$** | 3.46 | 21.93 | 20.84 | 7.02 | 82.61% |
| **$CO_2$** | 3.37 | 37.64 | 26.16 | 8.76 | 97.08% |

## 5 Implications

In this study, the interaction of $CO_2$-$H_2O$-coal systems were shown to ~~caused~~ change coal surfaces ~~to change~~ from water-wetting to intermediate-wetting. This determines

fluid flow and the pore-scale configuration of fluids, which and fluid flow, thereby further affecting reservoir-scale fluid dynamics. After $CO_2$ treatment, hvBb coal in the situ reservoir condition ($P$=120 bar, $T$=45°C) is favorable for $CO_2$-ECBM projects. In this case, reduced capillary forces favor $CO_2$ injection and percolation rate in coal seams (Sakurovs and Lavrencic, 2011; Arif et al., 2016b), resulting in a wider and more homogeneous distribution of $CO_2$ plume. $CO_2$ displacement efficiency is evaluated by capillary number $N_{ca}$, where larger contact angles makes $N_{ca}$ larger, i.e., water or methane is more easily displaced (Shojai Kaveh et al., 2011).

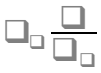

(12)

The wetting phase transition is also favorable to for overcome overcoming the water blocking effect (water as the wetting phase blocks the methane in the micropores) that occurs inaffects hydraulic fracturing technique (Li et al., 2022). $CO_2$, as the wetting phase, can enter the micropores and displace methane due to its stronger adsorption capacity (Pini et al., 2010).

However, this alteration is also imparts a detrimental to impact on $CO_2$ sequestration. $CO_2$ because storage capacity under caprock is assessed limited by the balance between capillary force and buoyancy balance,. and This balance limits the permanently immobilized $CO_2$ storage height $h$ immobilized permanently is derived (Iglauer, 2018).

(13)

Increasing contact angles indicate the decrease in storage capacity and containment security. The advancing and receding contact angles measured in this study truly reflect fluid migration processes such as displacement and flowback, and can be utilized to predict and improve field practices, including nanoparticles, surfactants, and polymers used to modify wettability (Ali et al., 2023).

## 6 Conclusions

We measured time-dependent dynamic and static contact angles (CA) on the coal surfaces exposed to $CO_2/N_2$- coal $H_2O$ by using the captive bubble method, with the nonaqueous phase in gaseous and supercritical states. We characterized physicochemical properties by FTIR, XRD, and SEM in order to analyze identify the mechanisms responsible for weakening water-wetting after $scCO_2$ treatment. The main conclusions are as follows.

(1) The contact angles (CAs) for gas and supercritical $N_2$ treatment only changed slightly. For gas $CO_2$gaseous $CO_2$ treatment, the dynamic CA also varied slightly. For $scCO_2$ treatment, both the static and dynamic CAs increased significantly, and the

636 average $\theta_{adv}$ changed from water-wet (27° for $scN_2$ treatment) to intermediate-wet
637 (92°).
638 (2) The chemical reactions of minerals resulted in inhomogeneous and rougher
639 surfaces with corrosion pores, connecting partially isolated pores, fracture extension,
640 and edge warping, finally generating greater contact angle hysteresis; all which favor
641 $CO_2$-wetting.
642 (3) The abundance of hydrophilic functional groups decreased while that of
643 hydrophobic functional groups increased following $scCO_2$ treatment. The unfavorable
644 water-wet changes were reflected in four aspects: the shedding of polar oxygen-
645 containing functional groups, the reduction of hydrogen bonds, elevated coal rank, and
646 increased percentage of hydrocarbons.
647 (4) $scCO_2$ treatment depleted most of the inorganic mineral components (most
648 notably calcite). The molecular polymerization of carbon was higher and crystallites
649 developed toward graphite-like growth and elevated coal rank. These changes in
650 crystallite structure are not favorable for water-wetting due to the higher carbon
651 content and lower surface charge.

652

## 653 CRediT authorship contribution statement

654 **Ke Li:** Investigation, Writing–original draft, Formal analysis, Visualization.
655 **Chuanjie Zhu:** Writing–review & editing, Methodology, Funding acquisition,
656 Supervision. **Jiamin Wan:** Writing–review & editing, Conceptualization,
657 Supervision, Resources. **Tetsu K. Tokunaga:** Writing–review & editing,
658 Supervision. **Na Liu:** Investigation. **Cong Ma:** Investigation. **Baiquan Lin:** Project
659 administration.

## 660 Declaration of competing interest

661 The authors declare that they have no known competing financial interests or personal
662 relationships that could have appeared to influence the work reported in this paper.

## 663 Acknowledgements

664 This work was supported by the National Natural Science Foundation of China
665 (NSFC) (Grant Number: 52174211); the National Science and Technology Major
666 Project (Grant Number: 2020YFA0711803); and the Key Program of the National
667 Natural Science Foundation of China (Grant Number: 52334007). This material is
668 also partly based upon work supported by the U.S. Department of Energy, Office of

Fossil Energy, Office of Natural Gas and Petroleum Technology, through the National Energy Technology Laboratory, under Award Number DE-AC02-05CH11231.

## Data availability

Data will be made available on request.

## References

Ali, Muhammad, Yekeen, N., Ali, Mujahid, Hosseini, M., Pal, N., Keshavarz, A., Iglauer, S., Hoteit, H., 2022. Effects of Various Solvents on Adsorption of Organics for Porous and Nonporous Quartz/CO2/Brine Systems: Implications for CO2 Geo-Storage. Energy Fuels 36, 11089–11099. https://doi.org/10/gst85h

Ao, X., Lu, Y., Tang, J., Chen, Y., Li, H., 2017. Investigation on the physics structure and chemical properties of the shale treated by supercritical CO2. Journal of CO2 Utilization 20, 274–281. https://doi.org/10/gbqwqq

Arain, Z.-U.-A., Aftab, A., Ali, M., Altaf, M., Sarmadivaleh, M., 2023. Influence of stearic acid and alumina nanofluid on CO2 wettability of calcite substrates: Implications for CO2 geological storage in carbonate reservoirs. Journal of Colloid and Interface Science 646, 567–575. https://doi.org/10/gst849

Arif, M., Al-Yaseri, A.Z., Barifcani, A., Lebedev, M., Iglauer, S., 2016a. Impact of pressure and temperature on CO2–brine–mica contact angles and CO2–brine interfacial tension: Implications for carbon geo-sequestration. Journal of Colloid and Interface Science 462, 208–215. https://doi.org/10/gst85c

Arif, M., Barifcani, A., Lebedev, M., Iglauer, S., 2016b. CO2-wettability of low to high rank coal seams: Implications for carbon sequestration and enhanced methane recovery. Fuel 181, 680–689. https://doi.org/10.1016/j.fuel.2016.05.053

Battino, R., Rettich, T.R., Tominaga, T., 1984. The Solubility of Nitrogen and Air in Liquids. Journal of Physical and Chemical Reference Data - J PHYS CHEM REF DATA 13, 563–600. https://doi.org/10/fs6ghq

Besford, Q.A., Christofferson, A.J., Kalayan, J., Sommer, J.-U., Henchman, R.H., 2020. The Attraction of Water for Itself at Hydrophobic Quartz Interfaces. J. Phys. Chem. B 124, 6369–6375. https://doi.org/10/gst84t

Bhutani, G., Khandekar, S., Muralidhar, K., 2012. CONTACT ANGLES OF PENDANT DROPS ON ROUGH SURFACES.

Boehm, H.P., 1989. Surface Properties of Carbons, in: Morterra, C., Zecchina, A., Costa, G. (Eds.), Studies in Surface Science and Catalysis, Structure and Reactivity of Surfaces. Elsevier, pp. 145–157. https://doi.org/10.1016/S0167-2991(08)60678-3

Cai, Z., Song, Y., 2021. Implementing Contact Angle Hysteresis in Moving Mesh-Based Two-Phase Flow Numerical Simulations. ACS Omega 6, 35711–35717.

https://doi.org/10/gst84w
Chaturvedi, T., Schembre, J.M., Kovscek, A.R., 2009. Spontaneous imbibition and wettability characteristics of Powder River Basin coal. International Journal of Coal Geology, CO2 Sequestration in Coals and Enhanced Coalbed Methane Recovery 77, 34–42. https://doi.org/10.1016/j.coal.2008.08.002
Chau, T.T., 2009. A review of techniques for measurement of contact angles and their applicability on mineral surfaces. Minerals Engineering 22, 213–219. https://doi.org/10.1016/j.mineng.2008.07.009
Chen, C., Wan, J., Li, W., Song, Y., 2015. Water contact angles on quartz surfaces under supercritical CO2 sequestration conditions: Experimental and molecular dynamics simulation studies. International Journal of Greenhouse Gas Control 42, 655–665. https://doi.org/10.1016/j.ijggc.2015.09.019
Chen, Y., Ma, D., Xia, Y., Guo, C., Yang, F., Shao, K., 2019. Study on wettability and influencing factors of different macroscopic components in low rank coal. Coal Science and Technology 47, 97–104. https://doi.org/10.13199/j.cnki.cst.2019.09.009
Crawford, R., Guy, D., Mainwaring, D., 1994. The influence of coal rank and mineral matter content on contact angle hysteresis. Fuel 73, 742–746. https://doi.org/10.1016/0016-2361(94)90018-3
Drelich, J., 2013. Guidelines to measurements of reproducible contact angles using a sessile-drop technique. Surface Innovations 1, 248–254. https://doi.org/10.1680/si.13.00010
Fatah, A., Bennour, Z., Mahmud, H.B., Gholami, R., Hossain, M., 2021a. Surface wettability alteration of shales exposed to CO2: Implication for long-term integrity of geological storage sites. International Journal of Greenhouse Gas Control 110, 103426. https://doi.org/10/gst846
Fatah, A., Mahmud, H.B., Bennour, Z., Hossain, M., Gholami, R., 2021b. Effect of supercritical CO2 treatment on physical properties and functional groups of shales. Fuel 303, 121310. https://doi.org/10/gst84n
Fuerstenau, D.W., Rosenbaum, J.M., You, Y.S., 1988. Electrokinetic behavior of coal. Energy Fuels 2, 241–245. https://doi.org/10/b6fmr7
Gathitu, B.B., Chen, W.Y., McClure, M., 2009. Effects of coal interaction with supercritical CO{sub 2}: physical structure. Industrial and Engineering Chemistry Research 48. https://doi.org/10/fw7mfg
Gensterblum, Y., Busch, A., Krooss, B.M., 2014. Molecular concept and experimental evidence of competitive adsorption of H2O, CO2 and CH4 on organic material. Fuel 115, 581–588. https://doi.org/10.1016/j.fuel.2013.07.014
Godoi, J.M., Matai, P., 2021. Enhanced oil recovery with carbon dioxide geosequestration: first steps at Pre-salt in Brazil. Journal of Petroleum Exploration and Production Technology 11, 1429–1441. https://doi.org/10.1007/s13202-021-01102-8
Guanhua, N., Qian, S., Meng, X., Hui, W., Yuhang, X., Weimin, C., Gang, W., 2019.

748 Effect of NaCl-SDS compound solution on the wettability and functional groups
749 of coal. Fuel 257, 116077. https://doi.org/10.1016/j.fuel.2019.116077
750 Hadi Mosleh, M., Sedighi, M., Vardon, P.J., Turner, M., 2017. Efficiency of Carbon
751 Dioxide Storage and Enhanced Methane Recovery in a High Rank Coal. Energy
752 Fuels 31, 13892–13900. https://doi.org/10.1021/acs.energyfuels.7b02402
753 Ibrahim, A.F., Nasr-El-Din, H.A., 2016. Effect of Water Salinity on Coal Wettability
754 During CO2 Sequestration in Coal Seams. Energy Fuels 30, 7532–7542.
755 https://doi.org/10/f85s3x
756 Iglauer, S., 2011. Dissolution Trapping of Carbon Dioxide in Reservoir Formation
757 Brine – A Carbon Storage Mechanism. https://doi.org/10.5772/20206
758 Iglauer, S., Mathew, M.S., Bresme, F., 2012. Molecular dynamics computations of
759 brine–CO2 interfacial tensions and brine–CO2–quartz contact angles and their
760 effects on structural and residual trapping mechanisms in carbon geo-
761 sequestration. Journal of Colloid and Interface Science 386, 405–414.
762 https://doi.org/10.1016/j.jcis.2012.06.052
763 Jia, Q., Liu, D., Cai, Y., Lu, Y., Li, R., Wu, H., Zhou, Y., 2022. Nano-CT
764 measurement of pore-fracture evolution and diffusion transport induced by
765 fracturing in medium-high rank coal. Journal of Natural Gas Science and
766 Engineering 106. https://doi.org/10/gst84s
767 Jung, J.-W., Wan, J., 2012. Supercritical CO2 and Ionic Strength Effects on Wettability
768 of Silica Surfaces: Equilibrium Contact Angle Measurements. Energy Fuels 26,
769 6053–6059. https://doi.org/10/f4bn9d
770 Kamble, A.D., Mendhe, V.A., Chavan, P.D., Saxena, V.K., 2022. Insights of mineral
771 catalytic effects of high ash coal on carbon conversion in fluidized bed Co-
772 gasification through FTIR, XRD, XRF and FE-SEM. Renewable Energy 183,
773 729–751. https://doi.org/10.1016/j.renene.2021.11.022
774 Kulinich, S.A., Farzaneh, M., 2009. Effect of contact angle hysteresis on water droplet
775 evaporation from super-hydrophobic surfaces. Applied Surface Science 255,
776 4056–4060. https://doi.org/10.1016/j.apsusc.2008.10.109
777 Labus, K., Bujok, P., 2011. CO2 mineral sequestration mechanisms and capacity of
778 saline aquifers of the Upper Silesian Coal Basin (Central Europe) - Modeling and
779 experimental verification. Energy, PRES 2010 36, 4974–4982. https://doi.org/10/
780 cqqgsn
781 Lerman, A., Mackenzie, F.T., 2018. Carbonate Minerals and the CO2-Carbonic Acid
782 System, in: White, W.M. (Ed.), Encyclopedia of Geochemistry: A Comprehensive
783 Reference Source on the Chemistry of the Earth, Encyclopedia of Earth Sciences
784 Series. Springer International Publishing, Cham, pp. 206–226.
785 https://doi.org/10.1007/978-3-319-39312-4_84
786 Li, K., Zhu, C., Liu, S., Chen, D., Cai, G., 2022. Effects of Injection Pressure and
787 Duration on Alternate High-Pressure Water-Gas Sequestration of Coalbed
788 Methane. Geofluids 2022, 1–15. https://doi.org/10.1155/2022/4563438
789 Liu, S., Yang, X., Qin, Y., 2010. Molecular dynamics simulation of wetting behavior at

CO2/water/solid interfaces. Chinese Science Bulletin 55, 2252–2257. https://doi.org/10/cs2cjj

Liu, S., Zhu, C., Li, Y., Hu, S., Zhang, X., Ma, C., 2023. Mechanism of adsorption capacity enhancement of coal due to interaction with high-pressure scCO2-water system. Gas Science and Engineering 117, 205080. https://doi.org/10.1016/j.jgsce.2023.205080

Liu, X., Sang, S., Zhou, X., Wang, Z., 2023. Coupled adsorption-hydro-thermo-mechanical-chemical modeling for CO2 sequestration and well production during CO2-ECBM. Energy 262, 125306. https://doi.org/10.1016/j.energy.2022.125306

Lu, Y., Tian, R., Liu, W., Tang, J., Li, H., Chen, X., Sun, X., 2021. Mechanisms of shale water wettability alteration with chemical groups after CO2 injection: Implication for shale gas recovery and CO2 geo-storage. Journal of Natural Gas Science and Engineering 90, 103922. https://doi.org/10/gst84m

MacInnes, D.A., Belcher, D., 1933. The Thermodynamic Ionization Constants of Carbonic Acid. J. Am. Chem. Soc. 55, 2630–2646. https://doi.org/10.1021/ja01334a003

Matlala, I.V., Moroeng, O.M., Wagner, N.J., 2021. Macromolecular structural changes in contact metamorphosed inertinite-rich coals from the No. 2 Seam, Witbank Coalfield (South Africa): Insights from petrography, NMR and XRD. International Journal of Coal Geology 247, 103857. https://doi.org/10.1016/j.coal.2021.103857

Ni, G., Li, Z., Sun, Q., Li, S., Dong, K., 2019. Effects of [Bmim][Cl] ionic liquid with different concentrations on the functional groups and wettability of coal. Advanced Powder Technology 30, 610–624. https://doi.org/10.1016/j.apt.2018.12.008

Pini, R., Ottiger, S., Storti, G., Mazzotti, M., 2010. Prediction of competitive adsorption on coal by a lattice DFT model. Adsorption 16, 37–46. https://doi.org/10.1007/s10450-009-9197-2

Reig, F.B., Adelantado, J.V.G., Moya Moreno, M.C.M., 2002. FTIR quantitative analysis of calcium carbonate (calcite) and silica (quartz) mixtures using the constant ratio method. Application to geological samples. Talanta 58, 811–821. https://doi.org/10/b5g7j2

Roshan, H., Al-Yaseri, A.Z., Sarmadivaleh, M., Iglauer, S., 2016. On wettability of shale rocks. Journal of Colloid and Interface Science 475, 104–111. https://doi.org/10/f8qd6k

Sabirzyanov, A.N., Il'in, A.P., Akhunov, A.R., Gumerov, F.M., 2002. Solubility of Water in Supercritical Carbon Dioxide 40.

Shang, L., Guanhua, N., Baisheng, N., Shouqing, L., Xijian, L., Gang, W., 2021. Microstructure characteristics of lignite under the synergistic effect of oxidizing acid and ionic liquid [Bmim][Cl]. Fuel 289, 119940. https://doi.org/10.1016/j.fuel.2020.119940

Shojai Kaveh, N., Barnhoorn, A., Wolf, K.-H., 2016. Wettability evaluation of silty

shale caprocks for CO2 storage. International Journal of Greenhouse Gas Control 49, 425–435. https://doi.org/10/f8pftv

Shojai Kaveh, N., Rudolph, E.S.J., Wolf, K.-H.A.A., Ashrafizadeh, S.N., 2011. Wettability determination by contact angle measurements: hvbB coal–water system with injection of synthetic flue gas and CO2. Journal of Colloid and Interface Science 364, 237–247. https://doi.org/10.1016/j.jcis.2011.07.091

Shojai Kaveh, N., Wolf, K.-H., Ashrafizadeh, S.N., Rudolph, E.S.J., 2012. Effect of coal petrology and pressure on wetting properties of wet coal for CO2 and flue gas storage. International Journal of Greenhouse Gas Control, CATO: CCS Research in the Netherlands 11, S91–S101. https://doi.org/10.1016/j.ijggc.2012.09.009

Siemons, N., Bruining, H., Castelijns, H., Wolf, K.-H., 2006. Pressure dependence of the contact angle in a CO2–H2O–coal system. Journal of Colloid and Interface Science 297, 755–761. https://doi.org/10/brm7zc

Sonibare, O., Haeger, T., Foley, S., 2010. Structural characterization of Nigerian coals by X-ray diffraction, Raman and FTIR spectroscopy. Energy 35, 5347–5353. https://doi.org/10.1016/j.energy.2010.07.025

Sun, E.W.-H., Bourg, I.C., 2023. Impact of organic solutes on capillary phenomena in water-CO2-quartz systems. Journal of Colloid and Interface Science 629, 265–275. https://doi.org/10.1016/j.jcis.2022.08.124

Sun, X., Yao, Y., Liu, D., Elsworth, D., 2022. How Does CO2 Adsorption Alter Coal Wettability? Implications for CO2 Geo-Sequestration. Journal of Geophysical Research: Solid Earth 127, e2021JB023723. https://doi.org/10/gqdg8j

Surface physical properties and its effects on the wetting behaviors of respirable coal mine dust, 2013. . Powder Technology 233, 137–145. https://doi.org/10/gnmxwz

Tenney, C.M., Cygan, R.T., 2014. Molecular Simulation of Carbon Dioxide, Brine, and Clay Mineral Interactions and Determination of Contact Angles. Environ. Sci. Technol. 48, 2035–2042. https://doi.org/10/f5sdxf

Tian, B., Qiao, Y., Fan, J., Bai, L., Tian, Y., 2017. Coupling Pyrolysis and Gasification Processes for Methane-Rich Syngas Production: Fundamental Studies on Pyrolysis Behavior and Kinetics of a Calcium-Rich High-Volatile Bituminous Coal. Energy Fuels 31, 10665–10673. https://doi.org/10.1021/acs.energyfuels.7b01788

Tokunaga, T.K., 2012. DLVO-Based Estimates of Adsorbed Water Film Thicknesses in Geologic CO2 Reservoirs. Langmuir 28, 8001–8009. https://doi.org/10/f3z83w

Tokunaga, T.K., Wan, J., Jung, J.-W., Kim, T.W., Kim, Y., Dong, W., 2013. Capillary pressure and saturation relations for supercritical CO2 and brine in sand: High-pressure Pc(Sw) controller/meter measurements and capillary scaling predictions. Water Resources Research 49, 4566–4579. https://doi.org/10.1002/wrcr.20316

Wan, J., Kim, Y., Tokunaga, T.K., 2014. Contact angle measurement ambiguity in supercritical CO2–water–mineral systems: Mica as an example. International

874 Journal of Greenhouse Gas Control 31, 128–137.
875 https://doi.org/10.1016/j.ijggc.2014.09.029
876 Wang, D.-B., Zhou, F.-J., Li, Y.-P., Yu, B., Martyushev, D., Liu, X.-F., Wang, M., He,
877 C.-M., Han, D.-X., Sun, D.-L., 2022. Numerical simulation of fracture
878 propagation in Russia carbonate reservoirs during refracturing. Petroleum Science
879 19, 2781–2795. https://doi.org/10/gst84r
880 Wang, H., Zhang, L., Wang, D., He, X., 2017. Experimental investigation on the
881 wettability of respirable coal dust based on infrared spectroscopy and contact
882 angle analysis. Advanced Powder Technology 28, 3130–3139.
883 https://doi.org/10.1016/j.apt.2017.09.018
884 Wang, Z., Wang, G., Hao, C., Ni, G., Zhao, W., Cheng, Y., Wang, L., 2023. Chemical
885 structure and hydrocarbon generation characteristics of tectonic coal with
886 different metamorphic degrees: Implications for gas adsorption capacity. Gas
887 Science and Engineering 112, 204949.
888 https://doi.org/10.1016/j.jgsce.2023.204949
889 Wei, J., Wang, H., Si, L., Xi, Y., 2022. Characteristics of coal-water solid-liquid
890 contact in gas atmosphere. Journal of China Coal Society 47, 323–332.
891 https://doi.org/10.13225/j.cnki.jccs.yg21.1707
892 Wu, J., Wang, J., Liu, J., Yang, Y., Cheng, J., Wang, Z., Zhou, J., Cen, K., 2017.
893 Moisture removal mechanism of low-rank coal by hydrothermal dewatering:
894 Physicochemical property analysis and DFT calculation. Fuel 187, 242–249.
895 https://doi.org/10.1016/j.fuel.2016.09.071
896 Xu, C., Wang, D., Wang, H., Xin, H., Ma, L., Zhu, X., Zhang, Y., Wang, Q., 2017.
897 Effects of chemical properties of coal dust on its wettability. Powder Technology
898 318, 33–39. https://doi.org/10.1016/j.powtec.2017.05.028
899 Xu, H., Zhu, Y., Liu, H., Ding, H., Fang, H., Zhang, K., Jia, J., 2023. Wettability
900 alteration and dynamic wetting behavior of coal during geologic CO2
901 sequestration using LF-NMR technology. Fuel 354, 129355.
902 https://doi.org/10.1016/j.fuel.2023.129355
903 Yan, J., Lei, Z., Li, Z., Wang, Z., Ren, S., Kang, S., Wang, X., Shui, H., 2020.
904 Molecular structure characterization of low-medium rank coals via XRD, solid
905 state 13C NMR and FTIR spectroscopy. Fuel 268, 117038.
906 https://doi.org/10.1016/j.fuel.2020.117038
907 Yan, J.-C., Bai, Z.-Q., Bai, J., Li, W., 2015. Chemical structure and reactivity
908 alterations of brown coals during thermal treatment with aromatic solvents. Fuel
909 Processing Technology 137, 117–123.
910 https://doi.org/10.1016/j.fuproc.2015.04.009
911 Yu, T., Li, Q., Li, X., Hu, H., Tan, Y., Xu, L., 2022. Synergistic effects of CO2 density
912 and salinity on the wetting behavior of formation water on sandstone surfaces:
913 Molecular dynamics simulation. Journal of Natural Gas Science and Engineering
914 105, 104714. https://doi.org/10.1016/j.jngse.2022.104714
915 Zhang, R., Liu, S., Zheng, S., 2021. Characterization of nano-to-micron sized

respirable coal dust: Particle surface alteration and the health impact. Journal of Hazardous Materials 413, 125447. https://doi.org/10/gpmj7s

Zhang, Y., Zheng, Y., Jiang, B., Yu, G., Ren, B., Yu, C., Wang, S., 2023. Experimental study on the influence of acid fracturing fluid on coal wettability. Fuel 343, 127965. https://doi.org/10.1016/j.fuel.2023.127965

Zhao, D., Liu, X., Shen, Z., 2023. Effect of oxygen-containing functional groups on the wettability of coal through DFT and MD simulation. Arabian Journal of Chemistry 16, 104606. https://doi.org/10.1016/j.arabjc.2023.104606

Zheng, S., Yao, Y., Elsworth, D., Liu, D., Cai, Y., 2020. Dynamic fluid interactions during CO2-ECBM and CO2 sequestration in coal seams. Part 2: CO2-H2O wettability. Fuel 279, 118560. https://doi.org/10.1016/j.fuel.2020.118560

Zhou, J., Zhang, J., Yang, J., Jin, Z., Luo, K.H., 2022. Mechanisms for kerogen wettability transition from water-wet to $CO_2$-wet: Implications for $CO_2$ sequestration. Chem. Eng. J. 428, 132020. https://doi.org/10.1016/j.cej.2021.132020

Zhu, C., Wan, J., Tokunaga, T.K., Liu, N., Lin, B., Wu, H., 2019. Impact of CO2 injection on wettability of coal at elevated pressure and temperature. International Journal of Greenhouse Gas Control 91, 102840. https://doi.org/10.1016/j.ijggc.2019.102840

## Appendix A. Supplementary material

**Table A. 1** Mineral compositions of raw coal

| Category | Common Minerals | Chemical formula |
|---|---|---|
| Silicate mineral (clay) | Kaolinite | $Al_4(Si_4O_{10})(OH)_8$ |
| | Illite (hydromica) | $K_{1-1.5}Al_4(Si_{7-6.5}Al_{1-1.5}O_{20})(OH)_4$ |
| | Chlorite | $(Mg,Fe,Al)_{12}[(Si,Al)_8O_{20}](OH)_{16}$ |
| | Montmorillonite | $(Na,Ca)_{0.33}(Al,Mg)_2(Si_4O_{10})(OH)_2{\cdot}nH_2O$ |
| | Muscovite | $KAl_2(AlSi_3O_{10})(OH)_2$ |
| Carbonate mineral | Calcite | $CaCO_3$ |
| | Siderite | $FeCO_3$ |
| | Dolomite | $CaMg(CO_3)_2$ |
| Oxide mineral | Quartz (chalcedony) | $SiO_2$ |
| | Hematite | $Fe_2O_3$ |
| Sulfide mineral | Pyrite, marcasite | $FeS_2$ |

**Table A.2** Fitting peak information in XRD for calculating semi-quantitative structural parameters

| Peak type | Group | FWHM | | | 2 (weighted average center) | | |
|---|---|---|---|---|---|---|---|
| | | γ-band | 002-band | 100-band | γ-band | 002--band | 100-band |
| Lorentz | Raw coal | 7.06641 | 3.38373 | 6.7259 | 21.07246 | 25.6866 | 40.01169 |
| Lorentz | $scN_2$ | 5.92757 | 3.86474 | 7.86542 | 20.81895 | 25.7018 | 39.43583 |
| Lorentz | $scCO_2$ | 10.75628 | 3.08301 | 4.65443 | 21.58649 | 26.39881 | 44.11167 |

**Table A.3** Dynamic contact angle under gaseous $N_2$ ($P$=20bar, $T$=25°C)

| Time (hours) | Left-Adv. | Right-Adv. | $\theta_{adv}$ | Left-Rec. | Right-Rec. | $\theta_{rec}$ |
|---|---|---|---|---|---|---|
| 0 | 28 | 28 | 28 | 24 | 23 | 23.5 |
| 24 | 33 | 31 | 32 | 23 | 22 | 22.5 |
| 48 | 29 | 30 | 29.5 | 25 | 19 | 22 |
| 72 | 31 | 27 | 29 | 26 | 19 | 22.5 |

| | | | | | | |
|---|---|---|---|---|---|---|
| 96 | 30 | 29 | 29.5 | 23 | 22 | 22.5 |

**Table A.4** Dynamic contact angle under $scN_2$ ($P$=120bar, $T$=45°C)

| Time (hours) | Left-Adv. | Right-Adv. | $\theta_{adv}$ | Left-Rec. | Right-Rec. | $\theta_{rec}$ |
|---|---|---|---|---|---|---|
| 0 | 29 | 28 | 28.5 | 21 | 21 | 21 |
| 24 | 29 | 28 | 28.5 | 22 | 21 | 21.5 |
| 48 | 26 | 23 | 24.5 | 20 | 17 | 18.5 |
| 72 | 28 | 25 | 26.5 | 22 | 20 | 21 |
| 96 | 27 | 26 | 26.5 | 21 | 21 | 21 |

**Table A.5** Time-dependent static CAs under $N_2$.

| Time | Average static contact angle (°) | |
|---|---|---|
| hours | gaseous $N_2$ | $scN_2$ |
| 0 | 24 | 23 |
| 24 | 25 | 22 |
| 48 | 24 | 23 |
| 72 | 23 | 24 |
| 96 | 23 | 23 |

**Table A.6** Dynamic contact angle under ~~gas $CO_2$~~gaseous CO2 (P=20bar, T=25°C)

| Time (hours) | Left-Adv. | Right-Adv. | $\theta_{adv}$ | Left-Rec. | Right-Rec. | $\theta_{rec}$ |
|---|---|---|---|---|---|---|
| 0 | 40.3 | 51.0 | 45.7 | 19.9 | 18.0 | 19.0 |
| 24 | 32.4 | 35.8 | 34.1 | 23.2 | 19.0 | 21.1 |
| 48 | 36.8 | 42.0 | 39.4 | 24.2 | 24.6 | 24.4 |
| 72 | 31.4 | 38.6 | 35.0 | 24.0 | 20.6 | 22.3 |
| 96 | 37.3 | 38.5 | 37.9 | 21.8 | 19.4 | 20.6 |

**Table A.7** Dynamic contact angle under $scCO_2$ ($P$=120bar, $T$=45°C)

| Time (hours) | Left-Adv. | Right-Adv. | $\theta_{adv}$ | Left-Rec. | Right-Rec. | $\theta_{rec}$ |
|---|---|---|---|---|---|---|
| 0 | 93.4 | 89.6 | 91.5 | 36.4 | 33.2 | 34.8 |
| 24 | 91.0 | 85.8 | 88.4 | 33.4 | 30.8 | 32.1 |
| 48 | 95.0 | 89.6 | 92.3 | 46.0 | 42.0 | 44.0 |
| 72 | 94.0 | 92.5 | 93.3 | 42.5 | 45.7 | 44.1 |
| 96 | 96.0 | 93.0 | 94.5 | 52.2 | 47.0 | 49.6 |

**Table A.8** Time-dependent static CAs under $CO_2$.

| Time(hours) | Static contact angle | |
|---|---|---|
| | ~~gas $CO_2$~~gaseous CO2 | $scCO_2$ |
| 0 | 22.5 | 35.0 |
| 24 | 22.0 | 44.2 |

| | | |
|---|---|---|
| 48 | 25.8 | 52.4 |
| 72 | 24.4 | 53.4 |
| 96 | 23.9 | 55.7 |

953